
Sorting atoms in spin-dependent optical lattices

Masterarbeit in Physik

von

Jonathan Zopes,

angefertigt im

Institut für Angewandte Physik,

**vorgelegt der Mathematisch-Naturwissenschaftlichen Fakultät der
Rheinischen Friedrich-Wilhelms-Universität Bonn.**

September 2014

Angefertigt im
Institut für Angewandete Physik
der Rheinischen Friedrich-Wilhelms-Universität Bonn

1. Gutachter: Prof. Dr. Dieter Meschede
2. Gutachter: Prof. Dr. Hans Kroha

Abstract

This work reports on the implementation of feedback methods for position control of single Cesium atoms in spin-dependent optical lattices. For this purpose a new control software has been developed. It encapsulates experimental control, fluorescence image acquisition and analysis into a single program. Combining the new software with spin-dependent transport and position-dependent addressing, we have developed a versatile feedback algorithm to deterministically arrange arbitrary patterns of up to 6 atoms. In addition, we have prepared two atoms in a common lattice site. We observed light-assisted collisions between both atoms and thereby characterized the preparation efficiency of $83 \pm 4\%$. The results pave the way for the study of controlled interactions between precisely two atoms in a single well of the optical lattice potential, enabling the realization of a fundamental quantum logic gate.

Contents

1	Introduction	1
2	Experimental Methods	3
2.1	Trapping single Cesium atoms	3
2.2	Qubits and their control	4
2.3	State-dependent conveyor belt	7
2.4	State and position detection	9
3	A novel control software	13
3.1	Motivation	13
3.2	Control systems for experiments with ultracold atoms	14
3.3	General architecture	17
3.4	Experiment control	18
3.5	Data management	23
3.6	Automatization methods	23
3.7	Summary	25
4	Sorting atoms in a state-dependent optical lattice	27
4.1	Addressing and transporting single atoms	27
4.1.1	Position-dependent microwave addressing	28
4.1.2	Transport efficiency analysis	32
4.2	Generating equidistant strings of atoms	34
4.2.1	Feedback mechanism	34
4.2.2	Results	39
4.2.3	Discussion	41
4.3	Preparing two atoms in a common lattice site	42
4.3.1	Experimental sequence	42
4.3.2	Results	43
4.3.3	Success rate of bringing two atoms to a common site	45
4.3.4	Discussion of light-induced one atom losses	49
4.3.5	Conclusion	51
5	Summary and Outlook	53
	Bibliography	55
	Acknowledgements	59

Declaration

61

1 Introduction

The field of quantum computation and simulation is based on the insight that certain classes of problems can only be solved by processors, which obey the laws of quantum mechanics. In the early 1980s these so-called quantum computers were proposed independently by Y. Manin [1] and R.Feynman [2], to facilitate simulations of many-body quantum systems. Classical computers are not efficient in this case due to the fact that the dimensionality of the Hilbert space describing the system increases exponentially with the number of particles involved. Hence storing the state vector of a system of N spin-1/2 particles, which is represented by 2^N complex amplitudes, requires an exponentially increasing amount of memory. In a quantum computer information is stored in (pseudo-) spin-1/2 systems called qubits. Storing the state vector of the system considered before is achieved by mapping it to a set of N controllable qubits. To process information stored in the qubits controlled interactions are required, that can be used to generate quantum logic gate operations or to mimic the effect of a specific Hamiltonian on the system [3].

Over the last two decades different possible architectures to realize a quantum computer or simulator have been proposed with qubits represented e.g. by atoms [4], ions [5], photons [6] or artificial two-level systems in superconducting circuits [7]. The challenge for experimental research teams is to gain precise control over the internal and external degrees of freedom of these microscopic or mesoscopic quantum objects and to implement tuneable interactions between them. Further the unwanted coupling to the environment, which leads to a decay of quantum superpositions, has to be minimized by working with cryogenic or vacuum setups.

Each of the architectures mentioned above has certain strength and weaknesses. Ions for example couple strongly with each other which helps to accomplish two-qubit gates. In fact the first quantum logic gate has been observed in a trapped ion system [8] and today up to 14 ions can be entangled [9]. At the same time ions couple also strong to the environment which leads to reduced coherence times. In addition the scalability of ion traps is very limited. Neutral atoms couple much weaker to their environment, hence in principle allowing for longer coherence times. The development of laser cooling, magneto-optical traps and optical lattices allows to store them in controllable and scalable potentials. However this comes at the price that controlled gate operations between the atoms are harder to realize because interatomic interactions are typically small. In 1998 D. Jaksch *et al.* proposed a scheme based on controlled cold collisions between two atoms trapped in the ground-state of separated but movable, state-dependent potential structures [10].

Depending on the initial qubit states of the atoms their trapping potentials are separated further or overlapped. The latter leads to a collisional phase shift that can be tuned by the interaction time to implement the desired gate. Experimentally this proposal has been realized with a many-body ensemble of Rubidium atoms in a state-dependent lattice in 2003 [11]. Until now a demonstration of this scheme with a single, controlled pair of atoms is still lacking.

The work presented in this thesis deals with the implementation of feedback schemes for the deterministic preparation of two Cesium atoms into a single site of a spin-dependent optical lattice. Combining this method with three-dimensional ground-state cooling, employing Raman and Microwave sideband transitions, will allow for the realization of controlled two-atom gates following Jaksch's proposal.

Outline

The remaining part of this thesis is structured as follows. In chapter 2 the experimental methods and the existing apparatus employed for the control of single, ultracold Cesium atoms is introduced. Chapter 3 describes a new control software for the experiment that has been developed to facilitate feedback control of atomic positions in the lattice. Finally, chapter 4 presents the results obtained with the new feedback algorithms. We have implemented methods to arrange atoms in equidistant strings and to prepare two atoms in a single site of the optical lattice. The preparation efficiency of both methods will be analyzed and discussed.

2 Experimental Methods

The feedback methods for position control investigated in this thesis require complete control of single Cesium atoms in their external and internal degrees of freedom and therefore over the experimental apparatus established in recent years. Hence the purpose of this first chapter is to give a short, but comprehensive overview of the experimental methods required to tame single atoms. Further details about the experimental apparatus can be found in the following PhD theses [12–14].

2.1 Trapping single Cesium atoms

The first step in all experiments conducted in our laboratory consists in pre-cooling a small ensemble of Cesium atoms in a magneto-optical trap (MOT). Subsequently the atoms are transferred into an one-dimensional optical lattice potential, which is formed by the interference of two counter-propagating laser beams. As the lifetime of the atoms in the optical lattice is limited by collisions with the thermal background gas a ultra-high vacuum environment is mandatory. In the given setup, the MOT and the optical lattice are therefore overlapped in a glass cell, in which the residual pressure is smaller than 1×10^{-10} mbar.

Magneto-optical trap

The dilute Cesium background gas in the vacuum chamber is in thermal equilibrium with the room temperature environment in the laboratory. In contrast the trap depth of the optical lattice is on the order of 1 mK. Hence the atoms need to be pre-cooled, before they can be transferred into the lattice potential. For this purpose the MOT mentioned above is used. It is capable of capturing Cesium atoms from the background gas and of cooling them to sub-millikelvin temperature. The working principle is based on a combination of velocity-dependent Doppler cooling and a magnetic quadrupole field, which adds a position-dependent force. More detailed informations on the physical mechanism can be found in the literature [15, 16].

In our experiment the MOT is operated on the Cesium D_2 line, with a wavelength of $\lambda_{D_2} = 852$ nm. The cooling transition is driven by an interference filter laser [17], that is spectroscopically locked to the $F=4 \rightarrow F=5$ transition. In addition a repumping laser on the $F=3 \rightarrow F=4$ transition needs to be operated to compensate off-resonant excitations to the $F'=4$ level, which can decay to the $F=3$ state.

The final temperature of the atoms is on the order of $125 \mu\text{K}$, such that they can be transferred into the optical lattice. A special property of the employed MOT is, that it is operated with a strong gradient of the magnetic quadrupole field and therefore small numbers of atoms can be trapped.

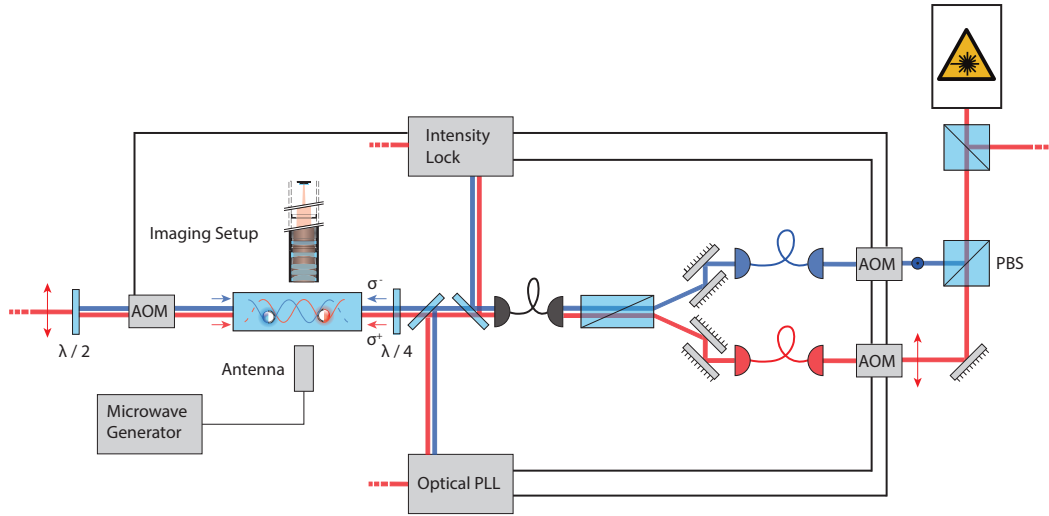


Figure 2.1: Sketch of the experimental setup, adapted from [18]. The optical elements, beams and coils for the magneto-optical trap are omitted here. The purpose of all further components, namely the intensity and phase stabilization of the optical lattice employing acousto-optic modulators (AOM), the microwave setup and the imaging system, is briefly described in this chapter.

Optical lattice

As mentioned before, the optical lattice is generated by the interference of two counter-propagating laser beams with wavelength λ_L . In the case of red-detuning to an atomic resonance, the light-matter interaction generates an attractive potential for the atoms at the maxima of the interference pattern, which has a periodicity of $\lambda_L/2$. The lattice beams are obtained from a Ti:Sa laser (Coherent MBR:110) and the intensity of the beams is locked with a feedback-loop controlled by acousto-optic modulators (AOM) to either 6 or 30 mW per arm (see figure 2.1). This corresponds to a trap-depth of $100 \mu\text{K}$ or $400 \mu\text{K}$, respectively. As will be discussed in section 2.3, we require the wavelength of the lattice laser to be $\lambda_L = 866 \text{ nm}$, to realize state-dependent potentials. In addition the polarization of the lattice beam, which enters the vacuum cell from the right hand side in figure 2.1, is synthesized for the state-dependent transport operations. This means that the phase of the σ^+ and σ^- -polarized components of the linearly polarized lattice are controlled with an optical phase lock loop (Optical PLL, see figure 2.1) employing the AOMs, as well.

2.2 Qubits and their control

In the previous section I described how a small ensemble of Cesium atoms can be cooled to sub-millikelvin temperature and subsequently transferred into an optical lattice potential with a periodicity of $\lambda_L/2 = 433 \text{ nm}$. This section elucidates how to extend the control, to the internal quantum states of the atoms. In practical

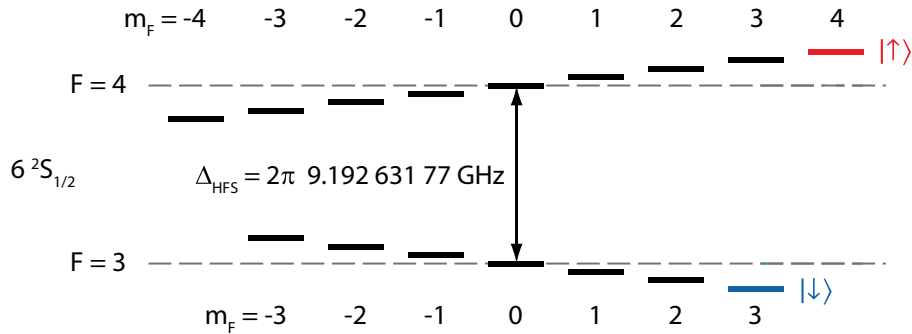


Figure 2.2: Hyperfine structure of the $6^2S_{1/2}$ ground-state of Cesium under the influence of a magnetic quantization field that shifts the levels due to the linear Zeeman effect. The qubit states $|\uparrow\rangle = |F = 4, m_F = 4\rangle$ and $|\downarrow\rangle = |F = 3, m_F = 3\rangle$ are highlighted.

applications it is highly desirable to reduce the Hilbert space of the internal states to an effective two-level system, such that the dynamics in external and internal degrees of freedom remain within reasonable degree of complexity and the two states can selectively be coupled by optical or microwave pulses.

In figure 2.2 the ground-state of Cesium is depicted, which comprises two long-lived hyperfine manifolds of degenerate magnetic sublevels, which we split by applying a magnetic quantization field of $|B_0| = 3$ G, orientated parallel to the optical lattice. Thereby the energy difference ΔE between subsequent m_F -levels in a given manifold accounts to approximately

$$\Delta E/\hbar = 2\pi \cdot 1.05 \text{ MHz.}$$

We select the outermost sublevels $|\uparrow\rangle = |F = 4, m_F = 4\rangle$ and $|\downarrow\rangle = |F = 3, m_F = 3\rangle$ as qubit states and combine optical m_F -pumping, to prepare $|\uparrow\rangle$ with high fidelity, with coherent microwave pulses to drive resonant transitions to the second qubit state $|\downarrow\rangle$ (see below).

State preparation by optical pumping

The optical pumping photons are extracted from the MOT cooling laser, which is locked to the only marginally off-resonant $F = 4 \rightarrow F' = 3, 5$ crossover transition. Before overlapping the optical pumping beam with the dipole trap, a combination of $\lambda/2$ and $\lambda/4$ plates generates the required σ^+ -polarization with very high purity, such that up to 99% of the atoms end up in the desired dark state $|\uparrow\rangle$. This fidelity was characterized by the state-selective push-out detection (see section 2.4). Whenever atoms decay to the $F = 3$ ground state, they are transferred back into the pumping cycle by a small fraction of MOT repumper photons overlapped with the optical pumping beam. The population lifetime $T_1 = 100$ ms of the $|\uparrow\rangle$ state is limited by spontaneous Raman scattering and orders of magnitude longer than microwave transitions and experimental sequences relying on the state preparation.

Coherent microwave transitions

We can obtain an arbitrary superposition of the two qubit states by driving coherent microwave transitions between the hyperfine levels. These are separated by approximately 9.2 GHz. In semiclassical approximation the dynamics of the two-level system driven by the microwave field can be described by the optical Bloch equations, which have been first studied by F. Bloch [19] in the field of Nuclear Magnetic Resonance (NMR) and which find rich applications in the study of many (pseudo-) spin-1/2 systems. While the two-level system is treated quantum mechanically, the radiation field is approximated classically.

The (pure) state $|\psi\rangle$ of the Cesium atom can be expressed by a superposition of the two hyperfine basis states

$$|\psi\rangle = \alpha |\uparrow\rangle + \beta |\downarrow\rangle. \quad (2.1)$$

The complex amplitudes α and β fulfill $|\alpha|^2 + |\beta|^2 = 1$. Hence by neglecting the global phase-shift γ one can map the current state $|\psi\rangle$ to a vector pointing onto the surface of the unit sphere in \mathbb{R}^3 . The vector is typically referred to as Bloch vector and allows for a simple, yet accurate illustration of the temporal evolution of the qubit (compare figure 2.3). The explicit expression for the Bloch vector

$$(u, v, w) = (\cos(\phi) \sin(\theta), \sin(\phi) \sin(\theta), \cos(\theta)), \quad (2.2)$$

is linked to the state of the atom by the relations $\alpha = \cos(\theta/2)$ and $\beta = e^{i\phi} \sin(\theta/2)$. Notice that the w component of the Bloch vector describes the population of the two-level system, while the u and v components describe the coherence properties. In classical dipole approximation the driving field can be written as

$$B = B_0 \cos(\omega t + \phi_{\text{rf}}) \quad (2.3)$$

The equations of motion in the rotating-wave approximation, which describe the temporal evolution of the components of the Bloch vector and thereby of the atomic quantum state can be expressed in compact vectorial form as

$$\dot{\mathbf{u}} = -\boldsymbol{\Omega} \times \mathbf{u} = -(\Omega_{\text{R}} \cos(\phi_{\text{rf}}), -\Omega_{\text{R}} \sin(\phi_{\text{rf}}), \delta) \times \mathbf{u}, \quad (2.4)$$

where we introduced the dipole moment d characterizing the coupling strength between atom and field, the detuning $\delta = \omega - \omega_0$ to the transition frequency and the Rabi frequency $\Omega_{\text{R}} = dB_0/\hbar$. Hence the driving field acts like a torque on the Bloch vector and rotates it in a plane defined by δ and Ω_{R} , while preserving the unit length of the vector. This evolution corresponds to the situation where no decoherence is present. In the following we will additionally assume that we drive resonant microwave pulses ($\delta = 0$), because we can calibrate the microwave frequency with microwave spectroscopy with high precision (see section 4.1.1). In this case we can identify two especially important pulse schemes that, starting from the optically pumped $|\uparrow\rangle$ state, allow us to prepare an equal superposition $\frac{1}{\sqrt{2}}(|\uparrow\rangle + |\downarrow\rangle)$ or a inverted population $|\downarrow\rangle$ (see figure 2.3).

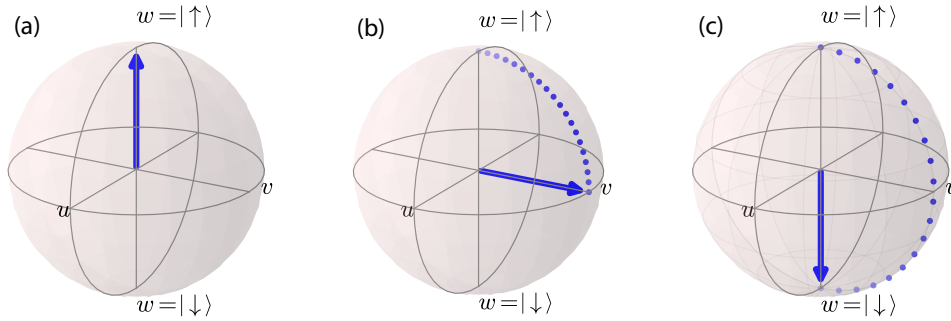


Figure 2.3: Graphical representation of the two-level system on the Bloch sphere. An initial state $|\uparrow\rangle$ (a) is transformed into an equal superposition state (b) or the inverted state $|\downarrow\rangle$ (c) by applying a $\pi/2$ - or π -pulse, respectively

The temporal evolution of the population component w of the Bloch vector, for constant Rabi frequency Ω_R and $\phi_{\text{rf}} = 0$, is given by (compare equation 2.4)

$$w(t) = -\cos(\Omega_R t).$$

Hence the population in the $|\downarrow\rangle$ state can be expressed as

$$P_{|\downarrow\rangle}(t) = \frac{C}{2}(1 - \cos(\Omega_R t)), \quad (2.5)$$

where the free parameter C is introduced to incorporate imperfections in the initialization and detection of the qubit states. The pulse schemes mentioned above, which allow us to prepare an equal superposition of the qubit states, or to invert the state are therefore realized for $\Omega_R t = \pi/2$ and $\Omega_R t = \pi$, respectively. Consequently these pulses are typically referred to as $\pi/2$ - or π -pulse. For time-dependent Rabi frequency the condition for a $\pi/2$ - or π -pulse generalize to $\int_{-\infty}^{\infty} \Omega_R(t) dt = \pi/2$ or π . In our experiment the microwave radiation at 9.2 GHz is generated by mixing radio-frequency signals at typically 160 MHz with a constant frequency of 9.04 GHz of a stable PLDRO oscillator. The radiation is emitted from a microwave antenna (see figure 2.1), located close to the vacuum cell and we achieve a maximum Rabi frequency of 50 kHz. We can generate temporally varying pulses by shaping the signal strength with a voltage-controlled-attenuator (VCA). Further details on the actual implementation, can be found in section 3.4.

2.3 State-dependent conveyor belt

Emergence of state-dependent potentials

The core feature of the experimental apparatus at hand is the state-dependent conveyor belt. It enables us to coherently transport atoms depending on their internal qubit state. In recent years this technique has been successfully used to observe quantum walks [20] and to realize a single atom interferometer [21].

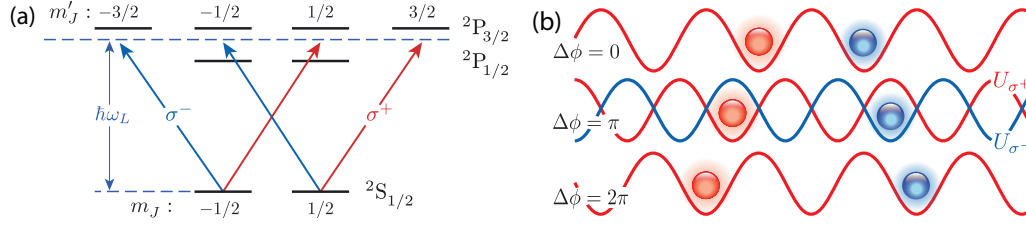


Figure 2.4: Schematic of the fine structure of Cesium (a) which exemplifies the emergence of state-dependent potentials. Further a visualization of state-dependent transport, realized by changing the relative phase $\Delta\phi$ between the σ^+/σ^- components of the lattice is depicted in (b). Adapted from [18].

The vectorial part of the AC-stark effect allows us to generate two superimposed optical lattice potentials, which to good approximation interact only with atoms in one of the qubit states. In a simplified, yet illustrative picture [12, 22], we consider parts of the Cesium fine structure, comprising the $^2S_{1/2}$ ground-state and the lowest lying excited states $^2P_{1/2}$ and $^2P_{3/2}$ (see figure 2.4). The transitions from ground-state to these excited states is conventionally termed D₁ and D₂ line with [23]

$$\lambda_{D_1} = 894.347 \text{ nm} \quad \lambda_{D_2} = 852.347 \text{ nm}.$$

Let us consider now, that we choose the wavelength of the laser generating the optical lattice such that it is located in between the D₁ and D₂ line. In addition the polarization of the optical lattice is chosen to be linear. Hence the the polarization vector can be written as an equal superposition of right and left circularly polarized light. As the magnetic quantization axis is collinear with the optical lattice these two polarizations drive only σ^+ or σ^- transitions, respectively. The fine structure term scheme shown in figure 2.4 suggests that for a properly chosen wavelength both $^2S_{1/2}$ levels

$$|\uparrow'\rangle = |j = 1/2, m_j = 1/2\rangle \quad |\downarrow'\rangle = |j = 1/2, m_j = -1/2\rangle,$$

couple only to the σ^+ or σ^- -component of the optical lattice because the opposing components vanish. This is the case because the attractive/repulsive Stark-effect contributions from the two excited states, cancel each other at the so-called magic wavelength. A rigorous calculation [22] taking into account further excited levels, in fact, yields a magic wavelength of

$$\lambda_L = 865.9 \text{ nm}. \quad (2.6)$$

However the fine structure levels $|\uparrow'\rangle$ and $|\downarrow'\rangle$ do not exactly map to the hyperfine qubit states that we are working with. The actual representation of the qubits in terms of hyperfine states leads to [22]

$$\begin{aligned} |\uparrow\rangle &= |I = 7/2, m_I = 7/2\rangle \otimes |\uparrow'\rangle \\ |\downarrow\rangle &= \sqrt{\frac{7}{8}} |I = 7/2, m_I = 7/2\rangle \otimes |\downarrow'\rangle - \sqrt{\frac{1}{8}} |I = 7/2, m_I = 5/2\rangle \otimes |\uparrow'\rangle. \end{aligned} \quad (2.7)$$

Hence the $|\uparrow\rangle$ -state couples purely to the σ^+ polarized component of the optical lattice potential, while the $|\downarrow\rangle$ -state experiences, apart from the dominant σ^- polarized component, also a small contribution from σ^+ .

Realizing state-dependent transport

The state-dependent potential is used to transport atoms depending on their qubit state. The spatial profile of each polarization mode σ^\pm formed of the counterpropagating laser beams in axial y -direction is given by

$$I_{\sigma^+}(y) \propto \cos^2(ky + \phi_+) \quad I_{\sigma^-}(y) \propto \cos^2(ky + \phi_-), \quad (2.8)$$

with the wave vector $k = 2\pi/\lambda_L$. Figure 2.4 (b) illustrates that changing the phase difference $\Delta\phi = \phi_+ - \phi_-$ between the two spin-dependent lattices leads to a spatial displacement of $\Delta y = \lambda/2 \cdot \Delta\phi/2\pi$ between them. Hence by independently controlling the phases ϕ_\pm , spin-dependent transport can be realized.

As mentioned in section 2.1 two *optical phase lock loops* (OPLL) are employed to actively control the phases ϕ_\pm . For this purpose a fraction of both polarization modes is extracted using a pick-up plate before entering the vacuum cell from the right hand side (see figure 2.1). Subsequently an error signal for each polarization mode is generated, by beating both with a common optical reference and comparing the phase of the beat signals with two independent, phase-stable electronic references in a phase-frequency discriminator. The error signals are then fed back to the drivers controlling the acoustic optical modulators, which ultimately steer the phase of the spin-dependent lattices. As the OPLL follows changes in the phase of the electronic references, the phases ϕ^\pm can be controlled. A complementary description elaborating more on the technical details of the feedback loop and its control is described in section 3.4. Further details on the implementation and characterization can be found in the following theses [24, 25].

2.4 State and position detection

Fluorescence imaging

The detection scheme in all of our experiments relies on fluorescence imaging of the atoms trapped in the optical lattice. Red-detuned molasses beams illuminate the atoms from all six spatial directions and provide further Doppler cooling. The detuning and intensity of the beams is optimized such that the maximum number of fluorescence photons can be extracted under the constraint that the survival probability of the atoms remains close to unity.

The fluorescence photons are collected with a diffraction-limited objective of moderate numerical aperture ($\text{NA} = 0.29$, see figure 2.1 or 2.5 (a)) and imaged onto a EMCCD detector (Andor iXon DV-887CS-FI) with a magnification factor of 55. The exposure time for a single fluorescence image ranges from 500 ms up to 2000 ms.

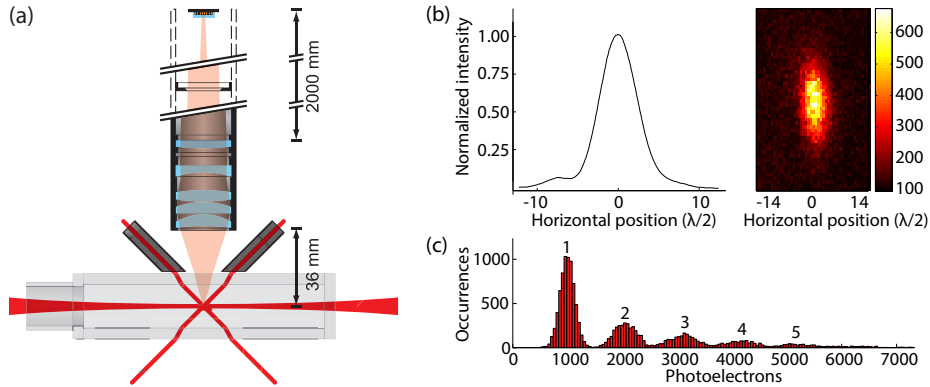


Figure 2.5: (a) Sketch of the imaging setup including the objective and the CCD chip. Adapted from [31]. (b) The extracted average line (vertically binned, left) and point (right) spread function of a single atom. (c) A histogram of fluorescence counts, used to determine the number of atoms present in an image by defining threshold conditions. The number above each peak represent the corresponding atom number.

Depending on the experiment that we want to perform we either count the number of atoms in a given image by means of threshold conditions (see figure 2.5) or we additionally deduce their positions. Thus distances of $\lambda_L/2 = 433 \text{ nm}$ have to be resolved optically, which according to Abbe's criterion [26, 27] would enforce the integration of high numerical aperture objectives ($NA > 0.7$) into the setup. Recently the research groups of M. Greiner and I. Bloch at Harvard University and the Max-Planck institute for Quantum Optics in Munich, respectively, have succeeded in integrating the first generation of such fluorescence microscopes into their experiments [28, 29]. In our group a similar objective has been developed [25] and is currently being tested [30].

In the existing setup we overcome the diffraction limit (horizontal resolution $4 \cdot \lambda_L/2$), by a numerical post-processing method called deconvolution [31]. It enables us to extract the position of the atoms in sparsely filled lattices with high fidelity $F \geq 0.95$. The deconvolution algorithm requires precise knowledge of the point spread function (PSF, see figure 2.5 (b)) of a single atom. It models the imaging process that converts the point-like atomic source into an intensity distribution, due to diffraction and aberration effects in the imaging system. More precisely the intensity distribution $I(x, y)$ on the detector is obtained by convolving the source distribution in the object plane $O(u, v)$ with the PSF

$$I(x, y) = (P * O)(x, y) = \int_{-\infty}^{\infty} \int_{-\infty}^{\infty} P(x - u, y - v) O(u, v) du dv.$$

The deconvolution algorithm attempts to recover the source distribution by numerically inverting the convolution, thereby obtaining the positions of the atomic emitters. Details on the numerical methods can be found in [12, 31].

State detection technique

To detect whether a microwave transition has occurred and hence to record for example microwave spectra or Rabi oscillations, a state-selective detection scheme is required. In our experiment this is realized by the so-called pushout - technique [32]. The MOT cooling laser tuned resonant to the $F = 4 \rightarrow F' = 5$ pushes atoms in the $F = 4$ state out of the optical lattice, while not affecting atoms in the $F = 3$ state. The mean survival probability of atoms in the $F = 4$ state is smaller than 1 %, whereas the probability for atoms in the $F = 3$ state is larger than 99 % [12].

3 A novel control software

In this chapter I will introduce a new control software for the experiment described in the previous chapter. It will be shown that this enables the development of feedback loops for sorting atoms in the state-dependent optical lattice and preparing precisely two atoms deterministically into a single site of the lattice potential (see chapter 4). It combines all functionalities of the previously exerted programs (see [12, 14]) for experimental control, data acquisition, and analysis in a single toolbox for Matlab. The general architecture of the software and the contained functionalities will be described in particular how the hardware devices are accessed and how experimental sequences can be generated and executed. I will also describe automatization routines contained in the software which reduce the maintenance requirements in the laboratory.

3.1 Motivation

The realization of controlled interactions between two atoms in a common site of the optical lattice requires two fundamental improvements of the existing setup. First, atoms have to be prepared in the three-dimensional ground-state of the trapping potential to ensure that measurable interaction phases are generated [33, 34]. For the longitudinal direction of the optical lattice a reliable cooling scheme exists. It is based on microwave sideband cooling in spatially displaced state-dependent potentials (see the corresponding publication [35] or dissertation [13]). Cooling in the transversal direction requires the implementation of a Raman laser system and an additional doughnut-shaped, blue-detuned trap into the setup. The additional trap increases the transversal confinement of the atoms such that Raman sideband cooling becomes feasible [34]. Secondly, we require a method to deterministically prepare two atoms out of the random initial distribution in the lattice in a controllable distance (see figure 3.1). Starting from this well-prepared initial state the application of the state-dependent transport would allow us to bring atoms in opposing qubit states to the same site where the interaction phase Φ_{int} can be acquired.

In recent years a method to imprint a controllable pattern of atoms employing magnetic resonance techniques has been developed in our group [36]. The method relies on the application of N spectrally narrow microwave π -pulses with frequency $\omega_1, \dots, \omega_N$ in a magnetic field gradient which introduces a position-dependent transition frequency. Initially the optical lattice is loaded with parameters optimized for high densities up to a filling of about 50% (limited by light-induced losses [36]).

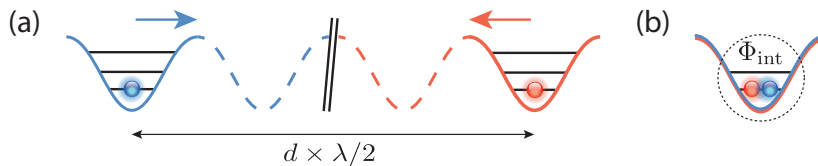


Figure 3.1: (a) Two atoms prepared in a well-defined distance d provide the starting point for experiments investigating controlled cold collisions in a common lattice site (b).

After optically pumping the atoms into the $|\uparrow\rangle$ state the addressing pulses are applied. The state of the atoms located at the sites P_1, \dots, P_N which are resonant with the pulse ω_i is inverted with highest probability. After the application of the microwave pulses the push-out technique is used to select only the addressed atoms. By repeating the method multiple times the preparation of atoms at the sites P_1, \dots, P_N reaches single-site precision.

In this thesis a different approach will be presented which instead of statically repeating a sequence of operations uses feedback methods which react on the current configuration of atoms in the lattice and adjusts it until the desired state is reached. One fundamental prerequisite for real-time feedback control of the atomic positions is that the control software allows to share information from the imaging system with the experimental control modules [37] and provides means to program feedback algorithms. In a previous work this was achieved by communicating between the existing stand-alone programs through a *named pipe* system, which allowed inter-program communication to synchronize the acquisition software of the EMCCD detector with the experimental control program [38]. However, this approach is unflexible. Further, during the implementation of this method the experiment was still operating with a transport scheme based on an electro-optical modulator (EOM) which constrained the attainable transport distances significantly [12, 14, 38]. In order to build up a more flexible scheme we decided to redevelop the complete software for the experiment.

3.2 Control systems for experiments with ultracold atoms

Electronic control systems are one of the key technologies for modern experiments with ultracold atoms. Most measurements are based on complex sequences of electronic signals which control laser beams, magnetic fields or microwave pulses with microsecond to nanosecond precision. A sequence is generated with special computer programs which provide interfaces to design, parse, and upload these to arbitrary waveform generators (AWG). The system of study is typically probed optically. Hence acquisition and analysis software for fluorescence or absorption imaging with CCD detectors is required. In many laboratories in-house developed software, specifically designed for the needs of the experiment, is in use [12, 32, 39, 40].

Legacy software

At the beginning of this thesis the following five stand-alone programs were employed in the experiment under study

- *Control Center*: sequence design and execution.
- *iXacq*: image acquisition and control for the EMCCD detector.
- *Wavegen*: pulse train upload to AWG for time precise trigger signals.
- *Vectorgen*: configuration of microwave generators.
- *H Terminal* (commercial): transport ramp programming.
- *Imaging Toolbox*: position reconstruction and data analysis.

All programs, apart from the commercial serial terminal software, were developed in our group. The first four programs that allow for the control of the experiment were written by former PhD student M. Karski. The *Imaging Toolbox* represents a Matlab extension that has been developed by A. Alberti and comprises most notably the capability to reconstruct the position of atoms from a given fluorescence image as described in [31].

Design choices and criteria for the new software

For multiple reasons we decided to implement the new control software in Matlab. First of all many hardware communication protocols or interfaces (Serial Port, GPIB, TCP/IP, VISA, etc.) are natively supported by Matlab's Instrument Control Toolbox. In addition it comprises a powerful script language with support for object-oriented programming which makes it less complex to generate programs when compared to C or C++. At the same time C functions can be executed using Matlab's MEX (*Matlab Executable*) interface if this is necessary for specific hardware libraries. For the given experimental apparatus this is the case for the core sequence control boards (see section 3.4) and for the EMCCD detector (see section 3.4). In addition the previously mentioned *Imaging Toolbox* is already available in Matlab and can hence be directly used.

In figure 3.2 the realized working principle of the control system for deterministic atom sorting is depicted. At each feedback operation a fluorescence image acquired by the EMCCD detector is transferred to the laboratory computer processed by means of position reconstruction and subsequently the control hardware of the experiment is configured for a suitable adjustment procedure. The manipulation of relative distances between the trapped atoms is based on a combination of position-dependent addressing and ensuing state-dependent transport. Therefore, both the microwave hardware and the lattice control system (described in section 3.4) have to be reprogrammed.

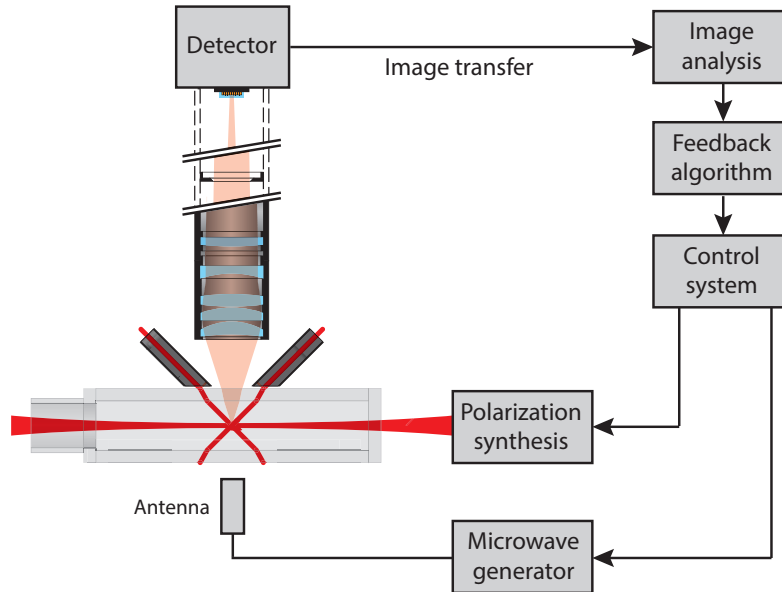


Figure 3.2: Illustration of the desired feedback control system. Trapped atoms are illuminated by optical molasses and a fluorescence image is acquired with an EMCCD detector. Subsequent digital deconvolution allows the reconstruction of atomic positions with single site resolution. The feedback algorithm selects a suitable reaction which is then programmed to the microwave and state-dependent transport control hardware.

Although the detailed implementation of the feedback algorithms is presented in chapter 4 it is clear that the processing and communication is realized in the most flexible and powerful way if the hardware interfaces, the sequence generation, and the data acquisition, as well as analysis are combined in one program.

Experiments with ultracold atoms are complex and based on many electronic and optical components that need to be operated at the same time. Hence, it is useful to automatize frequently conducted adjustment procedures, e.g. for the alignment of the orientation of the synthesized polarization vector (see section 3.6). In addition, we automatized frequently used calibration and characterization measurements like microwave spectroscopy or Ramsey interferometry (see also section 3.6).

In the legacy software the only measurement data that was automatically saved where the fluorescence images and the settings of the detector acquiring them. To improve on this we have implement a new data management system. The experimental settings of each measurement, the acquired fluorescence images, and the results of the analysis of the images are encapsulated into container objects (see section 3.5). This ensures that all relevant parameters for post-analysis of certain measurements can be retrieved.

3.3 General architecture

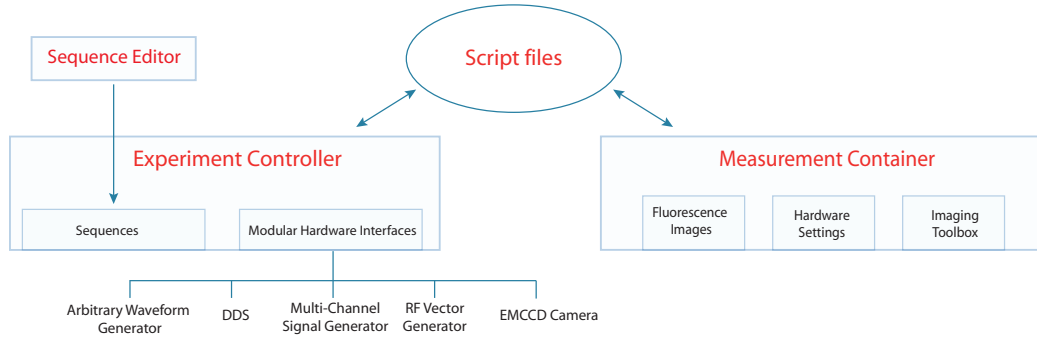


Figure 3.3: Schematic of the new control software. Details are given in the text.

In figure 3.3 the general architecture of the control software is depicted. It can be divided into two modules, the *experiment controller* and the *measurement container*. The modules are developed in an object-oriented way and while operating the control software one instance of the experiment controller and one instance of the measurement container class is present in memory.

The *experiment controller* provides the interfaces to the hardware components installed in the laboratory and thereby allows to configure these devices, e.g. to change the center-frequency of a radio-frequency generator or the acquisition time of the EMCCD detector. In addition, the experimental sequences which are designed with a graphical user interface (*Sequence Editor*, see section 3.4) are stored in the experiment controller in the form of matrices which contain the signals for analog and digital channels. Further, functions to execute these sequences or complex automation routines (see section 3.6) are part of the *experiment controller* class.

An instance of the *measurement container* class contains all relevant information of the specific measurement that it represents. As all information about the number, and position of the atoms is retrieved by fluorescence imaging the key information are the acquired fluorescence images. Apart from images further informations on the precise configuration of the hardware components are stored in the *measurement container* (see section 3.5).

Individual experiments (i.e. the measurement of a microwave spectrum) are written in script files that access and control the information and interfaces contained in both *experiment controller* and *measurement container*. In these script files complex logical decisions, based on the analysis of the acquired fluorescence images, lead to the implementation of feedback algorithms. In the following sections a more detailed description of both modules and the contained functionalities will be presented.

3.4 Experiment control

The following section describes the integration of the fundamental control hardware into the *experiment controller* module. Additional details on the experimental apparatus can be found in the corresponding PhD theses [12, 14, 25].

Central timebase and core control hardware

The core sequence is executed on three National Instruments (NI) cards, ($2 \times$ PCIe-6259, $1 \times$ PCI-6723) with a total number of 40 analog and 64 digital output channels and a maximum time-resolution of $2 \mu\text{s}$. Controlled parameters include laser intensities and frequencies, magnetic fields, and mechanical beam shutters. All timings that need to be more precisely controlled (e.g. microwave pulses) are delivered by arbitrary waveform generators from Agilent ($2 \times$ 33220A, $2 \times$ 33522A) with a time-resolution of up to 10 ns. The execution of the waveforms stored in the generators is triggered by the NI cards such that these cards deliver the central timebase for all experiments. The quality of the signals from the NI analog channels, especially of the PCI-6723 card, is in terms of RMS noise significantly inferior compared to the output of the Agilent devices and hence control quantities that rely on a low-noise steering signal need to be connected to the Agilent waveform generators as well.

Sequence generation and execution

Sequences are designed with a graphical user interface which has the form of a spreadsheet panel. The temporal behavior of each physical channel is represented by a row in the spreadsheet. Columns structure the sequence into blocks of certain purposes, e.g. ramping up magnetic fields or applying a microwave pulse. The duration of a block is the same for all channels. Entries for analog channels are interpreted as a combination of numerical numbers, pre-defined parser constants, and keywords for specific waveforms. Each entry is translated into samples using a self-written parser which currently supports linear, sinusoidal, polynomial or gaussian waveforms. The available waveforms can be easily extended if necessary.

The parser constructs a matrix with $M \times N$ entries that can be uploaded to the arbitrary waveform generators. Here M denotes the number of samples per channel in the sequence which is given by

$$M = S \cdot T_{\text{dur}},$$

with sample-rate S and total sequence duration T_{dur} . The signal generators can only run at constant sample-rate during a sequence. Further, each sample-point has to be supplied to the device even if the signal is constant over time. As we require the maximum time resolution of $2 \mu\text{s}$ during parts of the sequence we have to supply sample matrices with a typical size of $2 \cdot 10^6 \times 40$ corresponding to 40 registered analog and digital channels and $T_{\text{dur}} = 4 \text{ s}$.

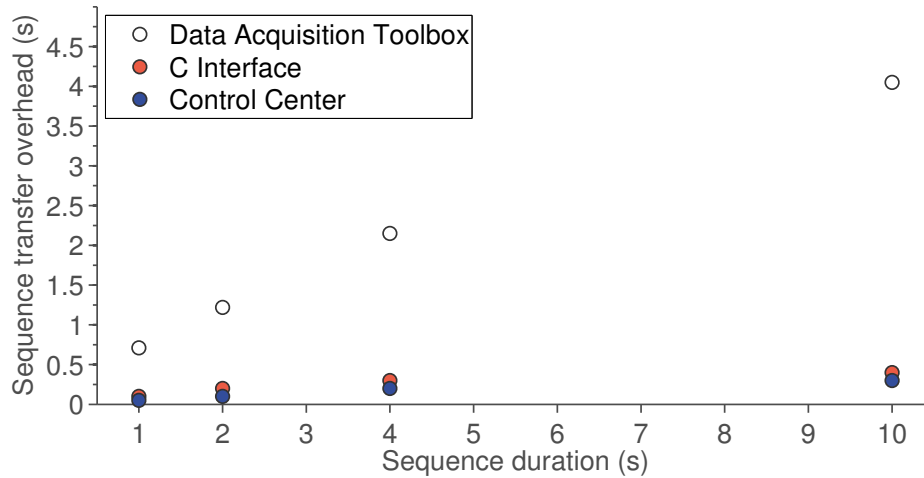


Figure 3.4: Comparison between the overhead introduced by transferring a sequence using the different interfaces discussed below. The error bars are smaller than the datapoints.

The transfer of the sequence from the laboratory computer running the control software to the NI cards is accomplished with a self-developed interface written in C. Initially we facilitated the Data Acquisition Toolbox which is a commercial extension of Matlab providing an interface to most available signal generator boards from National Instruments. However, we observed that the time overhead for transfer and execution of sequences amounted to almost 50% of the actual duration of the sequence. This means that 50% of the measurement time we would be waiting for the data transfer because the sequence needs to be transferred at each repetition.

We checked with the previously utilized sequencer *Control Center* that an overhead of less than 3% is typical using the native C libraries offered by National Instruments. Hence we decided to access the libraries using the MEX-interface which allows us to call C functions from the Matlab environment. The C interface was written in Visual Studio 11 and it supports the *Direct Memory Access* capabilities of the NI cards to ensure optimal performance.

The measured overhead for test sequences with durations between 1 and 10s is shown in figure 3.4. In each of the measurements 11 analog and 32 digital channels were registered to all three interfaces mentioned above. The sample rate was fixed to the maximum rate of 500 kSp/s. These settings correspond to the typical configuration for experiments. Evidently the implementation of the C interface reaches a performance in terms of sequence transfer overhead which is comparable to the one previous sequencer. The slightly lower performance is explained by the fact that at each transfer the whole configuration has to be rewritten to the NI cards. This includes trigger conditions, the routing of the sample clock, and the registration of analog and digital channels.

Microwave control system

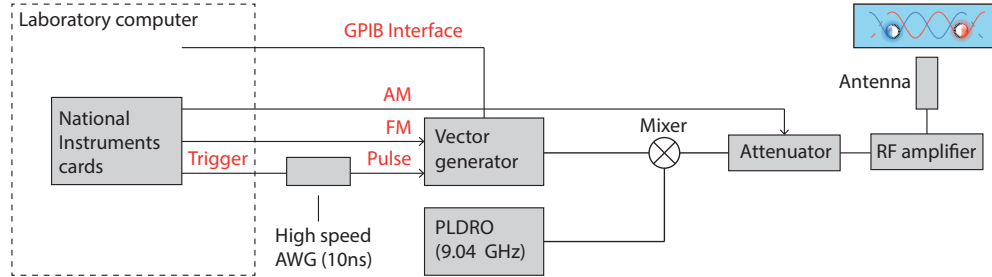


Figure 3.5: Sketch of the control hardware for the microwave setup.

The configuration of the hardware controlling and generating the microwave radiation is shown in figure 3.5. Instead of directly engendering the signal at 9.2 GHz a fixed-frequency signal from a *phase-locked dielectric resonator oscillator* (PLDRO) operating at 9.04 GHz is mixed with a variable radio-frequency signal at 160 MHz. The variable signal is generated by a vector generator (Agilent E4432B ESG-D) with a frequency range of 250 kHz to 3.3 GHz. The output of the vector generator can be pulse-modulated externally with a rising and falling time of 150 ns [12]. As mentioned in previous sections the time-resolution of the NI signal generators amounts to $2 \mu\text{s}$ which is not precise enough for microwave pulses with a typical Rabi frequency of 50 kHz. Therefore, the external pulse trigger of the vector generator is connected to an arbitrary waveform generator (Agilent 33220A) with a time resolution of 10 ns which itself is triggered by a NI card. Hence the duration of the pulses is controllable with 100 – 200 ns time resolution.

The vector-generator can be frequency-modulated (e.g. for microwave spectra) or phase-modulated (e.g. for Ramsey spectroscopy) by supplying an external analog modulation signal $U_m \in [0, 1] \text{ V}$. This signal is provided by the NI cards since we never require a better time-resolution than $2 \mu\text{s}$. Center-frequency, frequency modulation span, and amplitude of the signal from the vector generator can be programmed with a GPIB interface which is connected to the laboratory computer with a GPIB to ethernet controller. The commands to the GPIB port of the device are sent via the TCP/IP protocol to the controller and routed from there to the device. The protocol is supported by Matlab’s Instrument Control Toolbox (see section 3.4). To modulate the amplitude of the microwave pulses, e.g. for gaussian addressing pulses (see section 4.1.1), we use a PIN diode attenuator. The attenuation can be varied by a control voltage $U_a \in [0, 10] \text{ V}$. As the attenuation depends in a non-linear way from the control voltage each pulse modulation has to be modified with a calibration function to compensate the non-linearities. The calibration function has been characterized elsewhere [12]. After the attenuator the signal is amplified with a RF amplifier to an output power of up to 41 dBm (12.5 W) and guided to the microwave antenna placed close to the vacuum cell.

Lattice control system

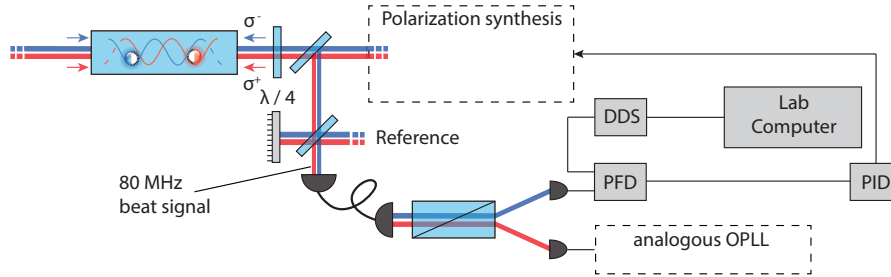


Figure 3.6: Sketch of the control hardware for one optical phase lock loop of the polarization synthesis.

The following paragraph extends the description of the polarization synthesis given in section 2.3 with complementary details on the control of the electronic reference signals. As described, the phase of the spin-dependent lattices and thereby their spatial position is stabilized using a beat signal with a common optical reference. The linear polarization modes of the beat signal, corresponding to the σ^+ and σ^- -polarized lattice, are separated in a Wollaston prism and thereafter separately detected with photodiodes. A phase-frequency discriminator (PFD) compares the phase of both electronic signals with a programmable electronic reference. The resulting output of the PFD serves as an error signal for a PID filter which generates a steering signal that itself is fed to a *voltage controlled oscillator* which drives an AOM controlling the phase of the σ^+ - and σ^- -polarized lattice thereby closing the feedback loop.

The reference is generated with a dual-channel direct-digital synthesizer (DDS, AD9954 [41]). Both channels of the DDS are locked to a single 400 MHz reference clock such that the controlled polarization modes are phase-stable to each other. The residual phase fluctuations of the locked system have been characterized to be below 1° RMS [24]. For transport operations the phase reference has to be ramped. If the ramp is slow enough, such that the lock can follow (Bandwidth ≈ 500 kHz), the corresponding lattice is translated with a temporal change of position defined by the form of the ramp (see section 4.1.2). The communication between the DDS and the control software is realized with a microcontroller (mbed LPC1768) using the SPI bus. A home-built box containing both devices, their connections, and the supply voltages has been developed by M. Genske and S. Brakhane [42]. The firmware of the microcontroller has been developed by A. Steffen and C. Robens [14, 25].

The communication between laboratory computer and the microcontroller programming the DDS has been implemented in Matlab using the serial interface. Apart from changing the configuration (e.g. frequency) of the DDS the microcontroller can either set a new phase for one of the output channels or program phase ramps into the memory of the DDS (compare section 3.4).

Device	Type	Purpose	Interface
Advantest R4131C	Spectrum Analyzer	Automized monitoring	Serial
Agilent 33220A	Arbitrary waveform gen.	Microwave pulse timing	USB
Agilent 33220A	Arbitrary waveform gen.	Transport timing	USB
Agilent 3522A	Arbitrary waveform gen.	Lattice depth control	USB
Agilent 3320B	RF vector-generator	Microwave pulses	Ethernet
Agilent N5182A	RF vector-generator	Raman lock reference	GPIB
Agilent 2024A	Oscilloscope	Automized monitoring	USB
Andor DV897	EMCCD detector	Fluorescence imaging	PCI
Marconi 2022C	RF generator	MW sideband cooling	GPIB
mBed LPC1768	DDS interface	Transport ramp upload	Serial
Newport 2835C	Powermeter	Lattice depth calibration	Serial
NI PCIe-6259	Multi-channel signal gen.	Main Sequence	PCIe
NI PCIe-6723	Multi-channel signal gen.	Main Sequence	PCI

Table 3.1: Alphabetically ordered list of hardware components implemented in the current version of the experiment controller module.

Once programmed the ramps are executed by triggering the microcontroller which instructs the DDS to execute the ramp. Up to four different phase ramps can be stored in the DDS at the same and for each of those a separate trigger input for the execution exists. However, the internal memory of the DDS can only store 1000 phase samples. This limitation can lead to non-smooth sampling of phase-ramps. To circumvent this problem an interface between a *field-programmable gate array* (FPGA) and the DDS is currently under development to transfer the phase during execution via parallel port.

Camera module

Fluorescence images are acquired with an electron-multiplied charged-coupled (EMCCD) detector (Andor iXon DV-887CS-FI). The vendor provides a software development kit (SDK) comprising a library of C functions which can be used to configure the device and transfer images to the laboratory computer. All required functions are accessed within Matlab using the MEX interface. An early version of the camera module has been developed by A. Steffen and I have extended upon his implementation. The device can be operated in continuous and kinetic mode. In the latter case the device can be triggered with an external TTL signal which in our case is provided by a digital output of the NI boards.

Summary

In summary, all relevant hardware devices installed in the laboratory are integrated into the software (see table 3.1 for a full list). In the following I will describe how, based on the interfaces, automatization and feedback procedures have been realized.

3.5 Data management

Property	Purpose
General settings	Data logging (type,date,comment string,etc.)
Sequence Log	Monitoring
Device settings	Data logging
Fluorescence images	Main read-out
Image analysis (*)	Position reconstruction, atom number estimation
Analysis module (*)	Data analysis e.g. Microwave spectrum analysis

Table 3.2: List of stored informations in each measurement object. The elements marked with an asterisk are classes that are part of the *Imaging Toolbox* developed by A. Alberti.

As mentioned in section 3.3, each single measurement is represented by a class that encapsulates all information of itself. For this purpose the current hardware configuration of the devices registered in the experiment module are synchronized with the measurement object before the data acquisition starts. In addition, all executed sequences are stored in a log file which is especially useful to post-analyze feedback decision of the control software. During the acquisition the fluorescence images are transferred to the measurement object and analyzed in real-time such that the experimentalist can immediately check the observations for consistency and can interrupt if they do not meet the expectations. Further the results of the analysis are also automatically stored in the measurement object.

3.6 Automatization methods

In this section automatized measurement and calibration methods will be described that have been implemented into the software in order to reduce maintenance requirements and error-proneness while setting up an experiment.

Automatized measurement procedures

A significant number of characterization measurements has to be performed on a frequent basis to ensure that the experiment is operated with optimal settings. Examples are the calibration of the qubit transition frequency using microwave spectroscopy or the efficiency of the push-out and optical pumping procedures. These measurement procedures are automatized in the new control software using script files as introduced in section 3.3. The scripting of procedures prevents errors during the configuration of devices and reduces the duration of setting up an experiment. Each script contains the whole measurement procedure including device configuration and real-time data analysis employing the *Imaging Toolbox*. The experimentalist can adjust the configuration and settings for the measurement in the header of the script file.

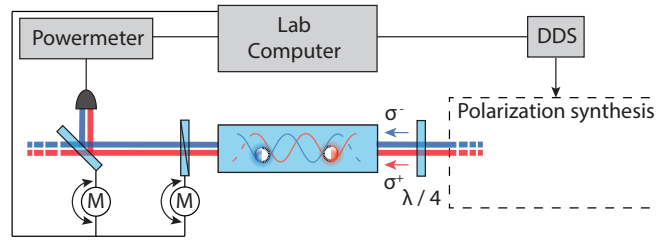


Figure 3.7: Sketch of the elements employed for the automatic alignment of the synthesized polarization vector. Details are given in the text.

A typical example is the adjustment of the center frequency of the microwave generator or the number of repetitions of a certain measurement. Currently the following fully automatized experimental methods are included in the software

- Survival, Pushout and Optical Pumping characterization
- Microwave and Raman spectroscopy
- Rabi oscillations
- Ramsey interferometry and T_2 measurements.

As described in section 3.5 the configuration of the experiment, and the acquired fluorescence images, as well as the results of the data analysis are automatically stored, encapsulated in a single *measurement container* object.

Automatized alignment procedures

Due to the complexity that the experiment has reached it is highly desirable to automatize regular adjustment procedures. One especially suitable procedure that will be presented as an example is the adjustment of the phase difference between the σ^+ and σ^- -polarized lattice. This ensures that the lattices are spatially overlapped. To achieve this experimentally the linear polarization of the synthesized polarization is overlapped with the linear polarization of the counter-propagating lattice beam. Figure 3.7 shows the schematic setup used for the automatic adjustment of the phase difference. Two motorized mounts (Thorlabs MFF101), controlled by TTL signals, can be flipped into the beam path of the optical lattice. The first flip-mount after the vacuum cell is equipped with a polarizer. It is oriented to be in extinction with respect to the polarization of the static lattice beam entering the vacuum cell from the left hand side. Therefore, the phase difference between both circular polarization modes of the synthesized lattice beam has to be adjusted such that the resulting linear polarization is in extinction with the polarizer. The second flip-mount is mounted with a mirror which extracts the transmitted intensity and guides it onto a powermeter (Newport 2835C). The measured intensity is transferred to the laboratory computer and serves as an input for a non-linear optimization algorithm (Nelder-Mead method, [43]) which varies the phase difference of the DDS reference until a minimum is reached.

3.7 Summary

In this chapter a novel control software has been presented that has been first and foremost developed to enable feedback methods for the spatial manipulation of atoms in the optical lattice. Based on a first version developed by myself the software was integrated in the experiment and extended in collaboration with PhD student C. Robens. The capabilities of the legacy software have been recovered and extended employing different hardware interfaces. Further automatized alignment and measurement procedures, and an advanced data management system have been implemented. The experiment has solely been operated with the new control software during the last 4 month and all results presented in the following chapter on sorting single atoms have been obtained using it.

In the future the new software can be used to apply closed-loop optimal control methods to our system. One could for example optimize the transfer efficiency and stability of microwave pulses against fluctuations in the transition frequency. This can be achieved by modifying the amplitude or phase modulation of the pulse such that e.g. the observed transfer efficiency is optimized. The fact that both data acquisition and experimental control are encapsulated in a single program allows for the implementation of such optimization loops.

4 Sorting atoms in a state-dependent optical lattice

In this chapter, I will present how we utilize spin-dependent transport, position-dependent addressing, and feedback methods employing the new software to generate arbitrary patterns of neutral atoms in the optical lattice. The efficiency to prepare equidistant strings of up to 6 atoms will be analyzed and compared to theoretical expectations. In addition, we have deterministically prepared two atoms in a common lattice site. Light-induced losses of atoms in the same site provide a clear signature of successful manipulations and allow us to characterize the preparation efficiency.

Our implementation thereby resembles a technologically improved version of the previously published *atom sorting machine* based on two crossed optical dipole traps [44, 45]. Further, the results pave the way for future experiments intended to study two-particle interferences or controlled interactions via cold collisions, directly realizing the entanglement proposal by D. Jaksch et. al. [33, 46].

The chapter is structured as follows. In the first section (4.1) the fundamental building blocks of all feedback operations will be described and characterized. The second section (4.2) describes a versatile feedback mechanism that has led to all results presented in this chapter. In addition, its application for generating equidistant strings of up to 6 atoms is analyzed. The final section (4.3) presents the main results of this thesis, the precise preparation of two atoms in a common lattice site.

4.1 Addressing and transporting single atoms

As mentioned above the intention of the first section of this chapter is to characterize the basic building blocks of the feedback mechanism, namely position-dependent addressing of single atoms and state-dependent transport to target locations. The combination of both methods allows us to manipulate the relative distance between atoms in the lattice and thereby to generate artificial patterns. In the first sections the position-dependent addressing of atoms in a magnetic field gradient will be discussed. Previous results on this topic, obtained at the experimental apparatus at hand, have been reported in the PhD thesis of M. Karski [12]. Further investigations on position-dependent addressing at a different experiment in our group can be found in the PhD thesis of D. Schrader [37] and the corresponding publication [47]. In addition, site-resolved microwave addressing employing the light-shift of a tightly focused laser has been reported for a two-dimensional Mott insulator state [48].

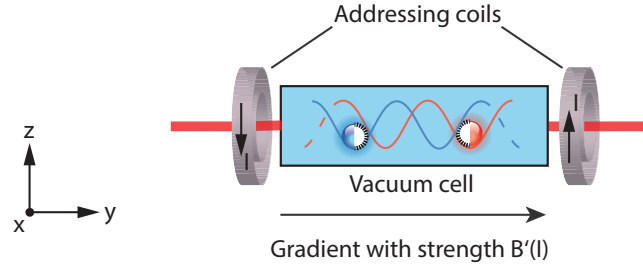


Figure 4.1: Configuration of the addressing coils in anti-Helmholtz configuration.

4.1.1 Position-dependent microwave addressing

To prepare two or more atoms in a pre-defined pattern we need to extend the experimental methods described in chapter 2 by position-dependent addressing of atoms such that state-dependent transport allows us to modify the relative distance between the atoms. For this purpose we apply a magnetic field gradient parallel to the direction of the optical lattice (y -direction) using a pair of coils in anti-Helmholtz configuration (see figure 4.1). Through these we drive a current of $I_{\text{grad}} = 4.1$ A. Due to the magnetic field gradient the microwave transition frequency ω between the qubit states becomes position-dependent according to [37]

$$\omega(y) = \Delta_{\text{HFS}} + \delta_0 + \Delta(y).$$

Here Δ_{HFS} represents the bare hyperfine splitting of $2\pi \times 9.2$ GHz, δ_0 gives the additional shift from the magnetic quantization field, and $\Delta(y)$ is the position-dependent contribution from the magnetic field gradient. On account of the linear Zeeman effect this contribution for magnetic gradient strength $B'(I)$ is given by [12]

$$\Delta(y) = \gamma B'(I) y,$$

with the gyromagnetic ratio $\gamma = (3g_3 - 4g_4)\mu_B/\hbar \approx 2\pi \times 2.5$ MHz/G. According to the gradient calibration method discussed in the following we obtain a shift of the transition frequency between neighboring lattice sites $\Delta(\lambda/2)$ of

$$\Delta(\lambda/2) = 2\pi \times (1.251 \pm 0.006) \text{ kHz}, \quad (4.1)$$

which in turn converts into a gradient strength of $B'(I = 4.1 \text{ A}) = 1.16 \text{ mG}/\mu\text{m}$.

Microwave addressing pulses

The magnetic field gradient will be constant in the subsequent analysis. Therefore, the spatial addressing resolution depends only on the spectral width of the applied microwave pulse. In figure 4.2 spectra for two different microwave pulse-shapes are shown. The spectrum on the left corresponds to a square pulse fulfilling the π -pulse condition. The pulse has a duration of $\tau_\pi = 9 \mu\text{s}$ applied with the maximum attainable Rabi frequency $\Omega_R = 2\pi \times 55$ kHz. The fourier-limited shape of the spectrum indicates two drawbacks of this pulse-scheme for application in position-dependent addressing.

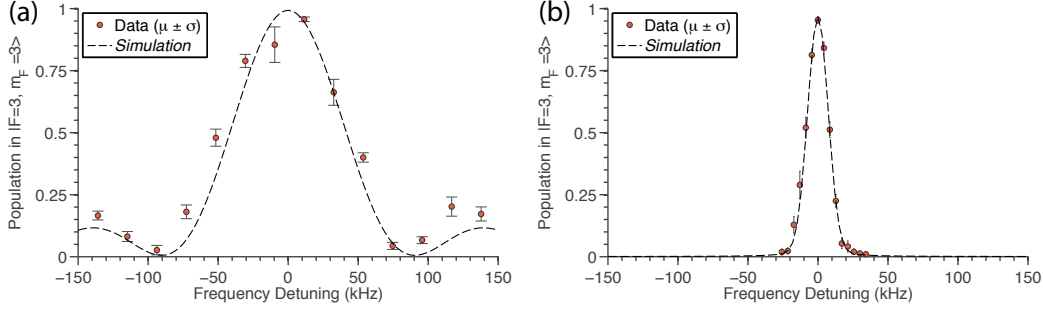


Figure 4.2: Microwave spectra obtained with a square pulse with $\Omega_R = 55$ kHz (a) and a Gaussian pulse ((b), compare eq. 4.2) with a $1/\sqrt{e}$ -width of $\sigma = 15$ μ s. The simulated spectra (dashed lines) are obtained by solving the damped Bloch equations with $T_1 = 100$ ms and $T_2' = 350$ μ s.

First the large spectral width $\Delta\omega_{\text{FWHM}} = 2\pi \times 96$ kHz leads to a low spatial resolution which secondly is further reduced by higher-order side-lobes. To circumvent this problem one could reduce the Rabi frequency of the square pulse and adjust the pulse duration such that the π -pulse condition is met again. Thereby, one can reduce the spectral width of the pulse but at the same time, due to the limited transversal relaxation time $T_2' = 350$ μ s, also the maximum achievable transfer is reduced. Further, the side-lobes still have to be taken into account.

Hence, instead of the square pulse we chose to use a pulse with Gaussian amplitude modulation

$$\Omega_R(t) = \Omega_0 \cdot \exp\left(-\frac{(t - t_{\text{pulse}}/2)^2}{2\sigma^2}\right), \quad (4.2)$$

with $1/\sqrt{e}$ -width of $\sigma = 15$ μ s and pulse duration $t_{\text{pulse}} = 150$ μ s = 10σ . The maximum Rabi frequency Ω_0 is adjusted such that the π -condition is fulfilled and the amplitude modulation is controlled by the voltage-controlled attenuator mentioned in section 3.4. The right panel of figure 4.2 shows the corresponding spectrum which is also of Gaussian-shape. In this case the spectral width amounts to $\Delta\omega_{\text{FWHM}} = 20$ kHz. The spatial resolution of the addressing pulse is proportional to the spectral distance between maximum transfer and the point where the transfer cannot be distinguished from the background of the spectrum, which is caused by the limited T_1 time and non-ideal state preparation and detection. In this thesis the threshold is set to 1% which for the Gaussian spectrum presented in figure 4.2 (b) leads to

$$\Delta_{\text{Addr}} = 30 \text{ kHz}.$$

Using $\Delta(\lambda/2)$ from equation 4.1 which converts a spectral resolution to a spatial resolution d_{MW} we obtain

$$d_{\text{MW}} = \Delta_{\text{Addr}}/\Delta(\lambda/2) \geq 16 \lambda/2,$$

which corresponds to a reasonable compromise between selectivity of the addressing pulse and transfer efficiency for the selected gradient current.

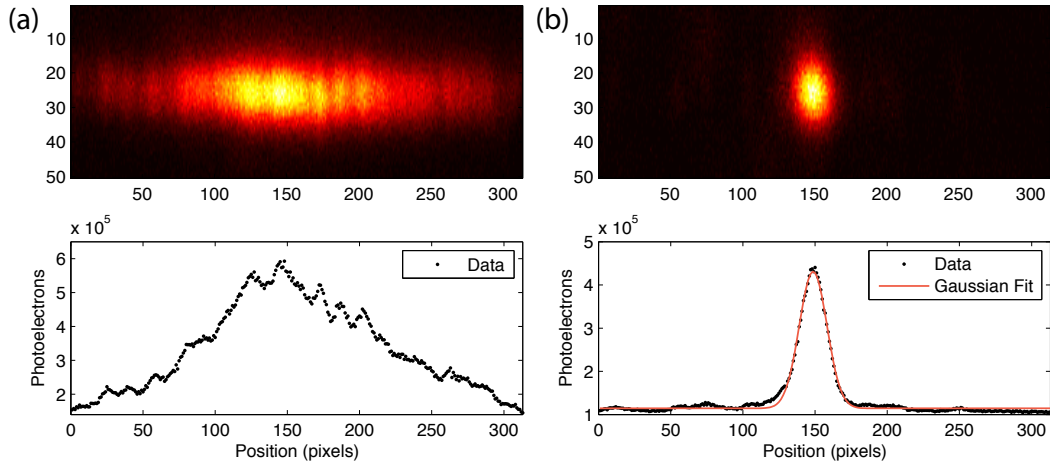


Figure 4.3: Illustration of the gradient calibration method. (a) Average over 20 fluorescence images of the initial population of atoms in the optical lattice. The loading duration of the MOT amounted to 20 s. (b) Average over 20 fluorescence images acquired after applying the position-dependent addressing and push-out to the initial populations.

Magnetic field gradient calibration

In the following I will describe how we calibrate the position-dependent transition frequency already used in equation 4.1 (see also figure 4.3). We start by loading the magneto-optical trap for a comparably long time of 20 s such that we can reach a high average filling of the optical lattice. Then we acquire a fluorescence image of the initial population of atoms. Subsequently we ramp up the magnetic field gradient and apply an addressing pulse. Thereafter we apply the state-selective push-out and acquire a second fluorescence image. After repeating this procedure for 20 times we average the final population in the lattice. Figure 4.3 (b) shows an example of the resulting average distribution of photoelectrons for a transition frequency resonant with atoms located close to the center of the fluorescence image.

The Gaussian distribution of the vertically binned photoelectrons (bottom-right panel) represents a microwave spectrum in position space (see for comparison figure 4.2 (b)). The center-position of the binned distribution, determined by fitting a Gaussian to the data points, allows us to estimate the position in the lattice with which the current addressing frequency is resonant. We repeat this process for various microwave frequencies. After several iterations the fitted central positions can be used to determine the magnetic field gradient as shown in figure 4.4. We extract the linear calibration function for the position-dependent addressing frequency by fitting the following linear function to the extracted central positions

$$\Delta\omega(y) = \Delta_0 + \Delta \cdot y$$

with Δ_0 being the frequency offset at left border of the camera field of view ($y = 0$) and Δ being the change of transition frequency per pixel in the field of view.

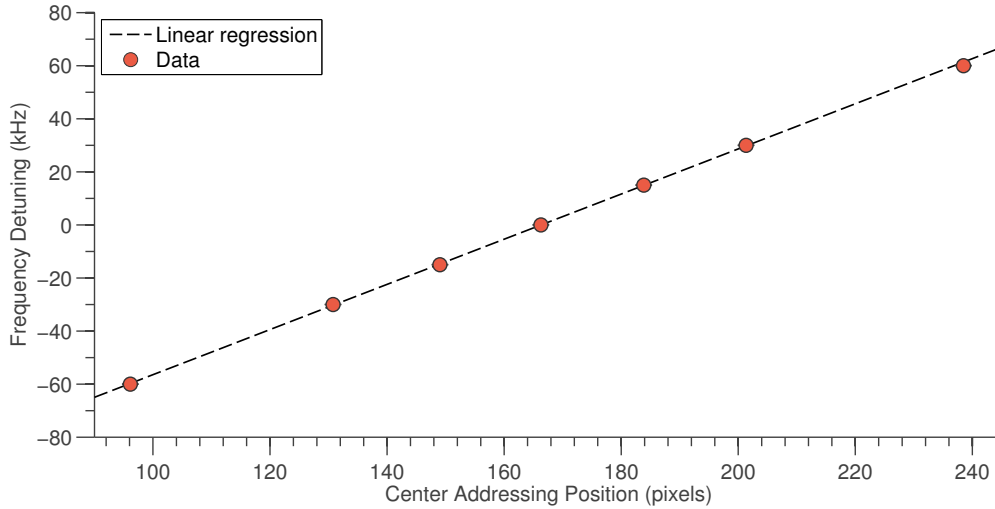


Figure 4.4: Resulting magnetic field gradient calibration for a current generating the gradient of 4.1 A. The resulting calibration parameters are discussed in the text below. The error bars are smaller than the data points.

For the measurement shown in figure 4.4 we obtained the following values

$$\Delta_0 = (-141.59 \pm 0.74) \text{ kHz} \quad \Delta = (851 \pm 4) \text{ Hz / Px}$$

Using the conversion factor η between pixels on the CCD detector and lattice sites in the object plane ($\eta = 1.471 \text{ px} / (\lambda/2)$) we obtain the slope per lattice site $\Delta(\lambda/2)$ with the result given in equation 4.1.

Automatized gradient calibration in the new control software

To ensure that the transfer efficiency of the Gaussian pulse is as high as possible the calibration has to be repeated before each measurement. We observed that the zero position of the magnetic field gradient drifts over several lattice sites within hours and therefore automatized the calibration method which can even be performed during measurements. In the software this is implemented via two functions

- Automatized measurement and analysis routine for the gradient calibration.
- Look-up function to retrieve the hardware control signals required for the desired transition frequency given the atom position, the current calibration, and hardware settings.

Based on these functions we can build up more sophisticated feedback schemes which rely on position-dependent addressing. Two schemes that have been developed during this thesis will be discussed in the following two main sections.

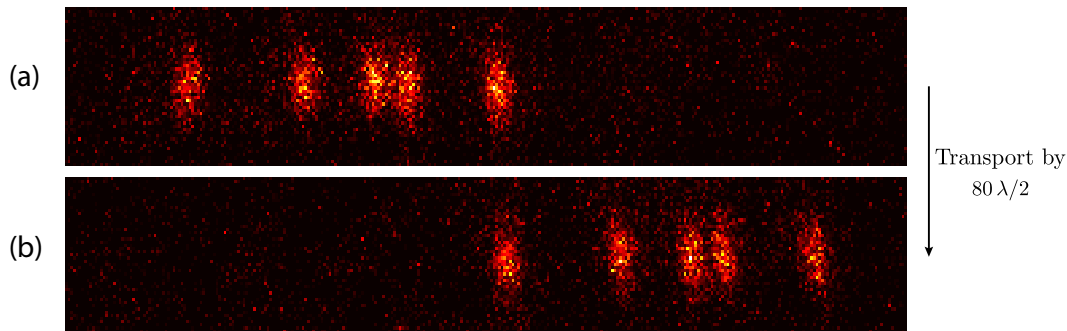


Figure 4.5: Illustration of the measurement procedure used to characterize the transport efficiency employing the polarization-synthesis setup. (a) Initial fluorescence image of five atoms. (b) After applying a global transport operation the atoms are shifted by $80 \lambda/2$.

4.1.2 Transport efficiency analysis

In this section the transport fidelity that we achieve with the polarization-synthesis setup will be analyzed. A description of the underlying physical implementation of the transport setup and control hardware is given in section 3.4.

All transport operations in this thesis have been obtained with cosinusoidal phase ramps which ensure that the atoms are smoothly accelerated such that no vibrational excitations are generated during transport. We have checked that this is the case by measuring sideband spectra of atoms after transport which have initially been prepared in the ground state of the longitudinal vibrational levels. Thereby we have observed that 98 % of the atoms remained in the longitudinal ground-state. The phase ramp P in degrees for a transport of N lattice sites, sampled with S sample points s_i is given by the following expression

$$P(s_i) = N \cdot 180^\circ \cdot (1 - \cos(\pi \cdot s_i/S + \pi)) + \phi_0 \quad (4.3)$$

with ϕ_0 being an initial phase offset. An example ramp is shown in figure 4.11 (b). The duration between updates of the samples in the DDS (see section 3.4) can be configured with a minimum duration and resolution of 10 ns. The control software automatically adjusts this duration, ensuring that the acceleration of the atoms is below a empiric threshold, which again ensures that no excitations are generated.

In order to characterize the transport precision the following measurement procedure has been used: Initially we load the optical lattice from the magneto-optical trap and adjust the loading time such that only a small number of atoms is transferred to the lattice. This ensures that the initial and final positions of the atoms can be numerically reconstructed with high fidelity. We optically pump the atoms trapped in the lattice into the $|\uparrow\rangle$ -state and then shift the σ^+ -polarized lattice using the phase ramp from equation 4.3. Hence, all atoms that have been successfully initialized in the $|\uparrow\rangle$ -state will be transported (see figure 4.5).

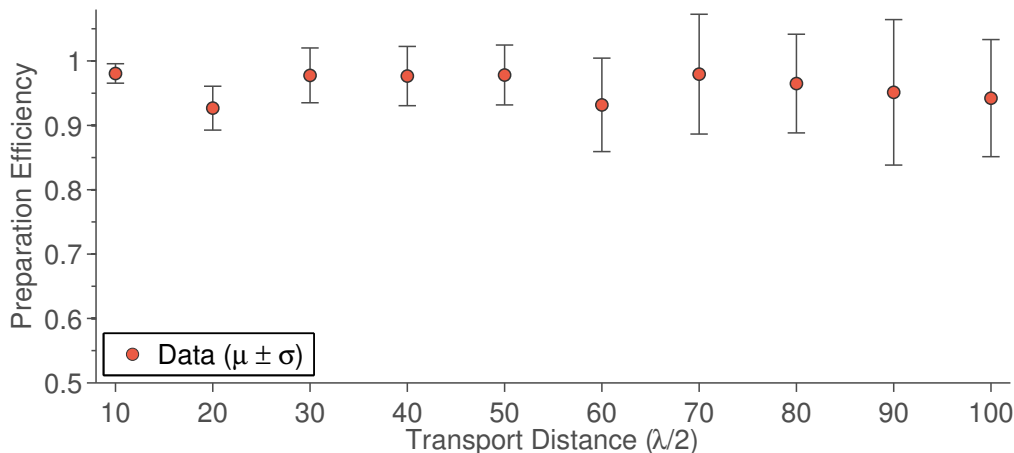


Figure 4.6: Probability to successfully transport atoms over target distances with an allowed tolerance of $\lambda/2$.

The transport distances amounted to multiples of $10 \cdot \lambda/2$ from 10 to 100 lattice sites. We have repeated this procedure 400 times for each of the transport distances. Afterwards we analyzed the probability with which the distance between the initial position of an atom and the final position matches with the transport distance within 1 lattice site. The obtained efficiencies are displayed in figure 4.6.

We had to attribute a tolerance of one lattice site in the following analysis because the position reconstruction precision has been non-ideal during the acquisition of this dataset. We have analyzed only those images in which the atoms were initially isolated by at least the transport distance d from the next neighboring atom. Hence, the number of useable images reduces significantly for larger transport distances as this restriction excludes more and more atoms which are separated by less than d . As a consequence the statistical uncertainties increase for larger transport distances. The average transport efficiency \bar{P} for distances between 10 and 100 lattice sites amounted to

$$\bar{P} = 96 \pm 2\%.$$

Hence, we can with certain qualifications rely on a precise transport mechanism in the following feedback techniques for pattern generation. The new polarization synthesis setup increases the range of accessible transport distances which was limited to 15 lattice sites with efficiency above 70% in the previous EOM setup (see [14]). In the future a more detailed analysis of the transport fidelity under ideal imaging conditions should be conducted to discriminate more precisely between errors due to non-correct detection and actual transport errors.

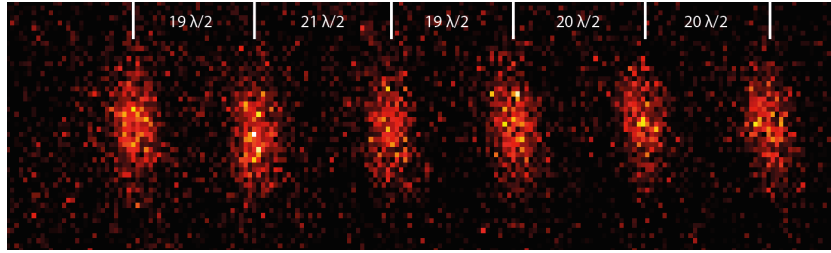


Figure 4.7: String of 6 atoms deterministically prepared with a target distance of 20 lattice sites and a tolerance of 1 lattice site for each of the inter-atomic distance.

4.2 Generating equidistant strings of atoms

Given the control over state-dependent transport and position-dependent addressing described in the previous sections sophisticated feedback schemes can be implemented that allow us to deterministically arrange patterns of atoms in the optical lattice. Apart from being a benchmark for the control system pattern generation might serve useful in the future for example to provide a starting distribution of atoms for experiments like interacting quantum walks. Further details on possible applications can be found in the outlook of this thesis.

4.2.1 Feedback mechanism

At the beginning of each attempt to generate the desired pattern we load the optical lattice with a loading-sequence optimized according to the following criteria

- The mean number of loaded atoms is ideally slightly higher than the required number of atoms for the pattern. We can adjust this parameter by changing the loading time of the MOT.
- The spread of the atoms is optimized to ensure addressability. For this purpose we turn off one of the arms of the optical lattice during the loading sequence. The atoms redistribute in the remaining running-wave trap which leads to a larger average spread.

Afterwards we enter the feedback loop which runs until we either reach the target pattern within the tolerance limits ($1 \cdot \lambda/2$ per separation, or no tolerance) or until the desired pattern cannot be generated anymore because the number of available atoms is lower than the number of atoms required to generate the pattern. During the feedback chain the following two steps are always executed subsequently

1. Determine a reaction given the current fluorescence image of the atoms in the optical lattice.
2. Generate and run an experimental sequence designed to achieve the required reaction and acquire a new fluorescence image.

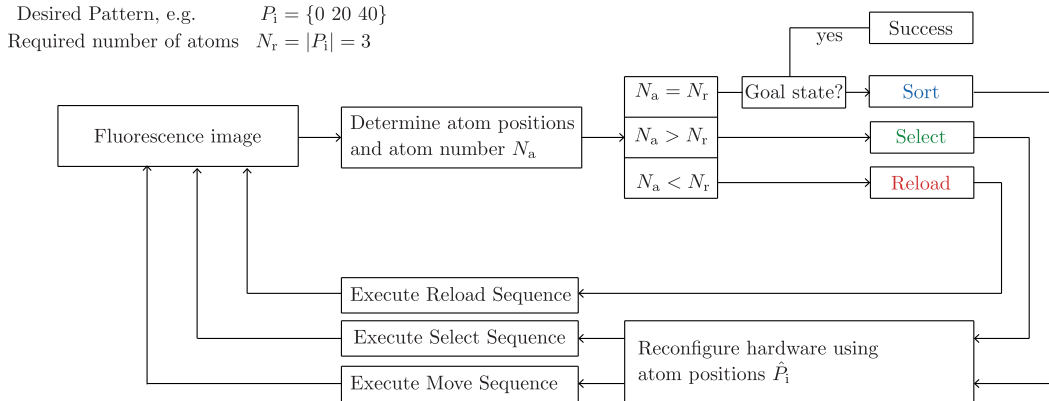


Figure 4.8: Schematic of the feedback algorithm, which determines a suitable reaction, based on the input parameters (fluorescence image, desired pattern).

In the following I will describe both steps in detail and how they are integrated into the control system. One should note at this point that the algorithm presented here, though representing a flexible and robust method to achieve the goal pattern, is not optimized in terms of overall efficiency or speed. Instead of compressing many addressing and transport steps into one experimental sequence we chose to apply each adjustment step one after another in single sequences.

Figure 4.8 shows a schematic which illustrates the functional principle of the feedback algorithm. As already mentioned before, we start with a fluorescence image of the current distribution of atoms in the lattice. While the algorithm is evaluating the image and reprograms the hardware, the atoms are stored in the lattice with activated molasses beams which provide further cooling. The lifetime in this case is limited by collisions with the thermal background gas in the vacuum cell and amounts to several minutes such that we can typically neglect any losses during feedback computations. The total number of atoms N_t and their positions P_i with $i \in \{1, 2, \dots, N_t\}$ are reconstructed using thresholding and numerical deconvolution (see section 2.4), respectively. The positions are sorted in descending order and the zero position is defined by the left border of the field of view.

Subsequently the separation of each atom to the neighboring one (if the atom is located at the outer right/left) or two atoms is calculated. Only atoms which are separated far enough from each other, such that they can be selectively addressed, can be manipulated and used to generate the pattern. Hence, the number of useable atoms N_a is given by all atoms that have a separation to neighboring atoms larger than the addressing resolution d_{MW} ($N_a \leq N_t$). Depending on the number of atoms required to generate the pattern N_r and the number of useable atoms N_a the feedback algorithm decides for one of the following reaction mechanisms

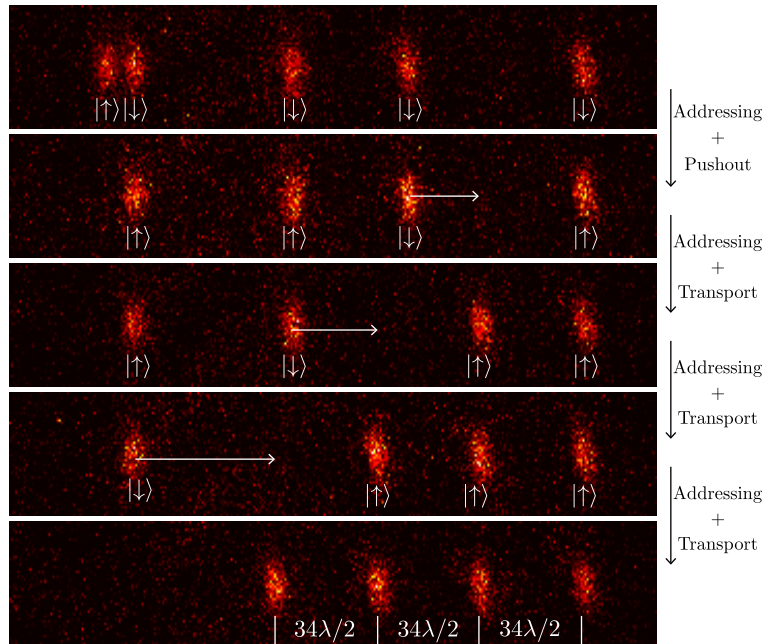


Figure 4.9: Exemplary feedback sequence for the preparation of an equidistant string of four atoms with a separation between the atoms of $34 \lambda/2$. The qubit state after preparation and manipulation steps are indicated below each of the fluorescence images.

1. $N_a < N_r$: The target cannot be reached and we need to reload the optical lattice to start with a new distribution.
2. $N_a > N_r$: In this case more atoms are available than we need to generate the pattern and therefore we need to select N_r atoms out of the N_a available.
3. $N_a = N_r$: Either a) The target state has been reached. Or b) Not all atoms are at the desired location. \rightarrow Sort with state-dependent transport.

Therefore the two non-trivial reactions are the selection of atoms and the actual adjustment of their positions by moving them with state-dependent transport. These will be discussed in the following. A graphical illustration of an exemplary feedback sequence is shown in figure 4.9.

Selection of atoms

The selection of atoms relies on a combination of position-dependent addressing and the pushout-scheme (see section 2.4). First all atoms are initialized in the $|\uparrow\rangle$ -state by optical pumping. Afterwards only the atoms that we want to keep/select are consecutively addressed with position-dependent Gaussian microwave pulses, employing the magnetic field gradient. The duration of a single gaussian pulse amounts to $t_{\text{pulse}} = 150 \mu\text{s}$ which is approximately three orders of magnitude smaller than the longitudinal decay time $T_1 = 100 \text{ms}$ of the qubit states.

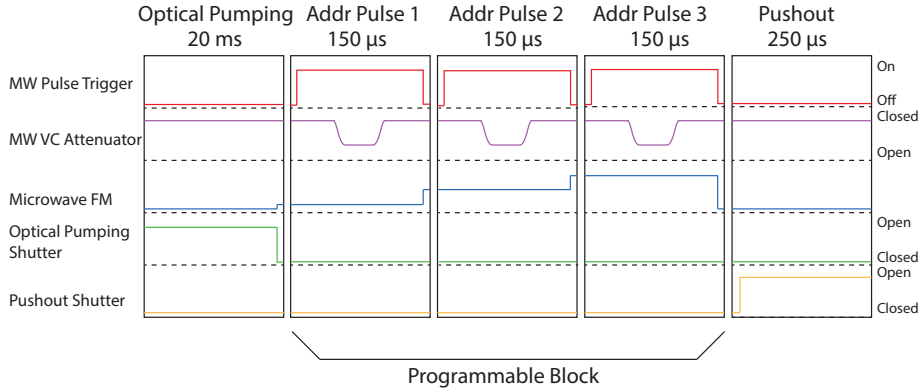


Figure 4.10: Representation of the programmable part of the select sequence described in detail in the in the text below.

Therefore the pulse duration is not a limiting factor for all currently accessible pattern sizes $N_r \leq 6$ (see section 4.2.2). Directly after the last addressing pulse we apply the pushout beam to keep only atoms which we have been addressed.

Sorting procedure

The generation of the actual pattern is achieved by moving one atom at a time to target. For this purpose the array of current positions P_i is compared to the target positions. As the absolute position of the pattern is not of relevance the position of the rightmost atom defines a reference position. The desired distances of the other atoms with respect to this reference position define the target positions. The first disagreement between current and target position will be corrected which means that the atoms to the right of the field of view will be moved first. Using the state-dependent transport only one atom is moved and the positions of the rest of the atoms is left untouched. Note that there exists one special case. If at least three atoms are initially less separated than it is desired but above the addressing resolution. In this case the algorithm might move multiple atoms instead of just one to ensure that all of them stay addressable. However, in practical applications this case does not occur frequently. After the optical pumping, a single addressing pulse is applied which is resonant with the position of the atom that needs to be moved. Subsequently the σ^- -polarized lattice for the $|\downarrow\rangle$ -state is shifted by the required number of lattice sites. Note that if all positions P_i correspond to the target positions, the algorithm will count the current attempt as a success and reload.

Programming the hardware

In the following the second step of the feedback chain, namely the generation and execution of the experimental sequence suitable for the reaction, will be described. The feedback algorithm returns the desired reaction and the corresponding transport distances and addressing positions to the control software.

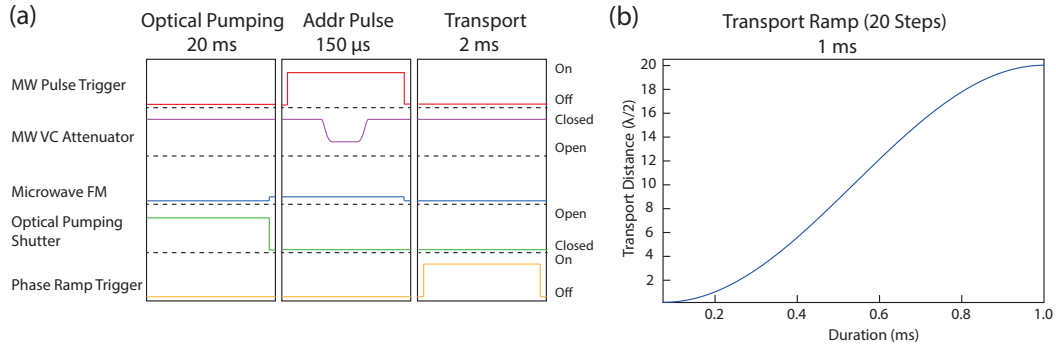


Figure 4.11: (a) Representation of the relevant and adjustable part of the sort sequence. (b) Example transport phase ramp for 20 lattice sites, according to equation 4.3.

Subsequently the addressing positions in pixels are converted to an analog signal for the frequency-modulation input of the microwave generator (see section 3.4). For this purpose the linear calibration function from section 4.1.1 is used. Depending on whether the select or sort procedure has to be applied the corresponding sequence is adjusted as follows. For illustration the programmable blocks of both sequences are shown in figure 4.10 and 4.11 (a), respectively.

In case of a selection procedure the feedback algorithm returns N_s addressing positions. After conversion to analog voltages, N_s subsequence-blocks are integrated into the select sequence. This is shown for $N_s = 3$ in figure 4.10. The amplitude modulation, controlled by the voltage-controlled attenuator, corresponds to the Gaussian addressing pulse which has been characterized in section 4.1. Note that the frequency modulation is constant during the application of each Gaussian pulse but changes between different pulses. Hence, atoms at different positions are addressed. In any case the atoms are optically pumped before the addressing operation and the push-out is applied afterwards.

In case of a sorting operation typically a single addressing frequency is returned for the one atom that needs to be moved. As discussed in the paragraph on the sorting procedure in rare cases multiple atoms need to be shifted. In that case multiple addressing frequencies will be returned. Subsequently the required number of addressing blocks will be integrated into the sequence. Figure 4.11 (a) shows the case that one atoms needs to be transported.

Apart from integrating the addressing block the DDS needs to be programmed for the transport phase ramp. In figure 4.11 (b) a typical phase ramp for 20 transport steps according to equation 4.3 is depicted. The control software automatically generates the required ramp and uploads it to the DDS via the microcontroller interface discussed in section 4.1.2. In any case the atoms are again optically pumped before the addressing operation and the transport operation is executed with a reserved maximum duration during the sequence of 2 ms.

4.2.2 Results

N	Preparation Distance ($\lambda/2$)	Attempts	Goal state reached	Fraction (%)
2	25	1500	723	48.2
3	34	500	84	16.8
4	34	1000	84	8.4
6	20 ± 1	4871	5	0.1

Table 4.1: Observed success fractions for the generation of equidistant strings of atoms.

The feedback method described in the previous section has been used to generate equidistant strings of $N \in \{2, 3, 4, 6\}$ atoms. The preparation distance between neighboring atoms varied between 20 and 34 lattice sites. In total 7871 repetitions have been measured distributed between the different string sizes N . The results of the measurement as well as the detailed settings are shown in table 4.1.

The efficiency to reach the goal pattern can be decomposed into two contributions. First, we consider the case that we start with a number of atoms that is larger than the number required to reach the goal state. In this case the feedback algorithm will react with an attempt to select a suitable subset of the available atoms. This procedure is successful with a fidelity $F_{\text{select}}(N)$ which depends on the number of atoms that we want to select. More specifically the fidelity can be expressed as

$$F_{\text{select}}(N) = A^N S^N, \quad (4.4)$$

with S representing the survival probability for a single atom per manipulation and A being the addressing fidelity again for a single atom. Note that the state initialization and the pushout-technique are assumed to be ideal here. If selecting the required number of atoms is successful the sorting procedure starts which reaches the target state with a fidelity of F_{sort} (see below).

The second contribution to the overall efficiency takes into account that the initial number of atoms already equals the required number without the necessity to apply the select procedure. In this case only the sorting fidelity F_{sort} has to be considered. By attributing the relative frequencies f_{select} and f_{sort} to the two possible contributions the total probability or efficiency to generate the desired pattern $E(N)$ can be written as

$$E(N) = F_{\text{sort}} \cdot (f_{\text{sort}} + f_{\text{select}} \cdot F_{\text{select}}). \quad (4.5)$$

The sorting fidelity F_{sort} can be decomposed by considering the different scenarios that can occur. As the initial position of rightmost atom defines the reference position for all other atoms, $N - 1$ successful transport operations have to be applied to reach the goal state. In special cases more than one atom has to be addressed and transported (see section 4.2.1) but this happens rarely and we can therefore neglect the corresponding contribution to the fidelity.

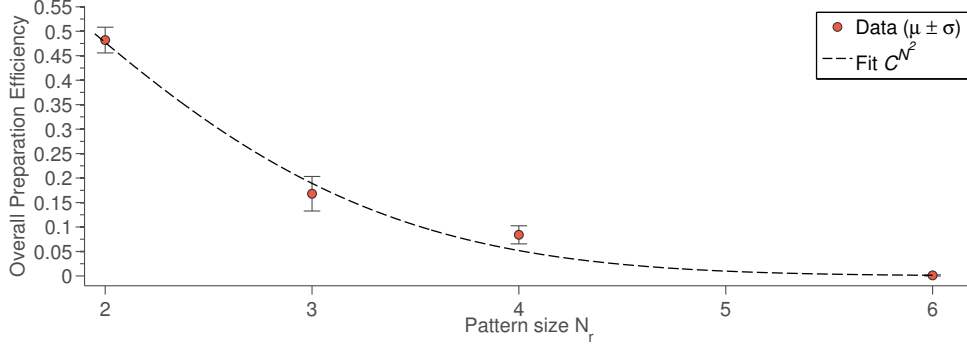


Figure 4.12: Super-exponential decay of the overall efficiency to generate a pattern consisting of $N \in \{2, 3, 4, 6\}$ atoms with an overall uniform spacing $\geq 20 \times \lambda/2$.

The sorting operations are successful with probability $S^N \cdot A$ under the assumption that transport errors can be neglected. With probability $S^N \cdot (1 - A)$ the addressing fails but all atoms remain in the lattice. In this case the feedback system will retry to apply the same sorting procedure and the combined success probability for this scenario is given by $S^N \cdot (1 - A) \cdot S^N \cdot A$. Hence, by considering also higher order cases, where the algorithm repeats the very same sorting procedure multiple times, we obtain for the overall sorting fidelity

$$\begin{aligned}
 F_{\text{sort}}(N) &= (S^N \cdot A + S^{2N} \cdot (1 - A) \cdot A + S^{3N} \cdot A \cdot (1 - A)^2 + \dots)^{N-1} \\
 &= \left(S^N \cdot A \cdot \sum_{k=0}^{\infty} (S^N (1 - A))^k \right)^{N-1} \\
 &= \left(S^N \cdot A \cdot \frac{1}{1 - S^N (1 - A)} \right)^{N-1}.
 \end{aligned}$$

Therefore, we have gained theoretical model that includes the scaling of the selection and sorting fidelities depending on the pattern size N , the addressing fidelity A , and the survival probability S . The scaling of the relative frequencies f_{sort} and f_{select} can only be determined by measurement. In principle they can be optimized for each specific pattern size N by adjusting the loading duration of the MOT.

To check the measured data for consistency with the model expressed by equation 4.5 both survival probability S and addressing fidelity A have been extracted from the measured data for each single pattern size N . The obtained values can be found in table 4.2. The survival probability has been deduced by the number of cases in which a single atom remained in the lattice during a sorting operation. Subsequently the addressing fidelity has been estimated from the number of successful selection operations according to equation 4.4. The significantly enhanced addressing fidelity in the case of $N = 2$ can be attributed to the fact that during this specific measurement the gradient calibration procedure was repeated for multiple times to ensure the best possible addressing accuracy.

N	$f_{\text{sort}} + f_{\text{select}}$	Addressing Efficiency A	Survival S	F_{theo}	F_{meas}
2	79%	86(1)%	95(1)%	49(1)%	48(1)%
3	62%	80(2)%	92(1)%	16(1)%	17(1)%
4	37%	77(3)%	95.5(4)%	9(1)%	8(1)%
6	7%	77(3)%	93.6(3)%	0.3(3)%	0.10(5)%

Table 4.2: Overview of the fidelities involved in the atom sorting routine. The confidence limits are obtained by the Clopper-Pearson method ($\alpha = 0.32$).

Inserting the estimates for S and A with the measured values for f_{sort} and f_{select} into our model from equation 4.5 leads to a theoretical prediction F_{theo} for the overall pattern generation fidelity. Again the results can be found in table 4.2. They show, within the uncertainties, agreement with the measured fidelities which confirms that the underlying main mechanisms have been correctly identified and suggests that no further mechanisms are present that significantly reduce the fidelity.

4.2.3 Discussion

In summary, this section comprises the experimental realization of a feedback algorithm which enables us to deterministically generate patterns of atoms in the optical lattice. In realistic applications the attainable pattern size is currently limited to $N \leq 4$. For larger pattern sizes the super-exponential decay of the generation efficiency makes the use unpractical (see figure 4.12).

We have observed that the addressing relies critically on the frequent calibration of the magnetic field gradient. For this purpose we have completely automatized this procedure and can even schedule it in between measurements. One possible future improvement might be the integration of addressing pulses with a spectral flat-top profile (e.g adiabatic passages) which are less sensitive to drifts of the magnetic field gradient while preserving the spectral selectivity [49].

In this thesis the addressing resolution was limited to $16 \lambda/2$. This limitation can in principle be overcome by increasing the current generating the magnetic field gradient. The installed power supply can deliver up to 45 A which would result in a resolution of approximately $2 \lambda/2$ for the given addressing pulse.

The method can be used to generate starting distributions for quantum walks. This could increase the repetition rate in the case of non-interacting walks if the atoms are initially prepared such that their position distributions after the walk cannot overlap. In the case of interacting quantum walks the procedure is even more relevant as it can be used to deterministically prepare the desired initial separations of the interacting walkers. In addition, the technique may even be used to generate the initial distribution of atoms for a qubit-gate array.

4.3 Preparing two atoms in a common lattice site

4.3.1 Experimental sequence

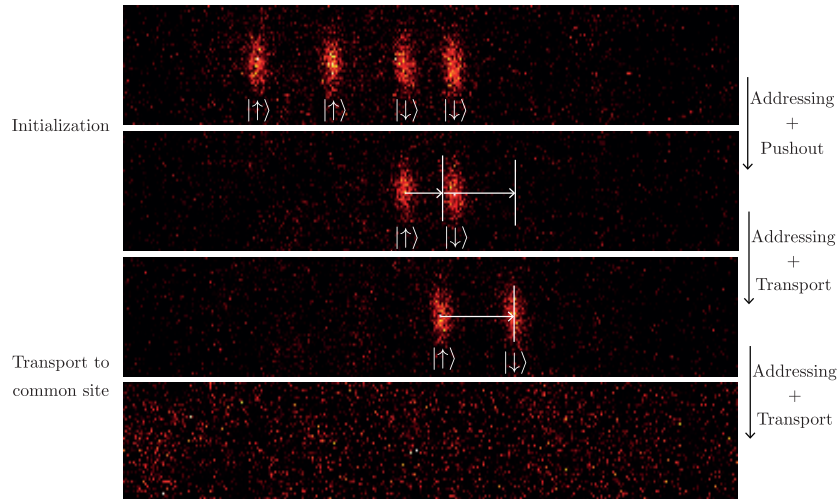


Figure 4.13: Exemplary feedback sequence for the preparation of the initial distribution for a light-assisted collision experiment and the sequence bringing the atoms together.

The experimental sequence to bring two atoms to a common lattice site comprises of two stages that will be described in the following. An additional illustration in terms of fluorescence images of a typical realization is depicted in figure 4.13.

In the first stage we generate a pattern of two atoms in a distance of $25 \cdot \lambda/2$ using an adapted version of the feedback mechanism described in section 4.2.1. Recall that in the previous applications the rightmost atom defined the reference position of the pattern and the remaining atoms were positioned such that desired distances between the atoms were realized. This was justified by the fact that only the distance between the atoms matters for the pattern and the absolute position in the field of view was not of relevance. In addition we could reduce the number of required sorting operations, as only $N-1$ atoms need to be sorted to achieve a pattern of N atoms.

The adaption consists in preparing the atoms always at the same positions. As the optical lattice is never perfectly parallel to the surface of the imaging objective and the molasses illumination is inhomogenous, the performance of the imaging system varies across the field of view. Hence, the positions have been selected by optimizing the brightness of the atoms in terms of fluorescence counts to ensure optimal position reconstruction. This reduces the probability to transport both atoms into neighboring instead of a common site. Further, the desired starting positions can be realized with one successful sorting operation by addressing one atom and then shifting both state-dependent potentials instead of just one. Hence, if initially two or more atoms are present, we apply the select- and the adapted sort-procedure subsequently or directly the latter one.

When two atoms are prepared in the desired starting positions the second stage of the experiment is executed. Namely, the atom on the left starting position is addressed and transported to the position of the atom on the right. In fact, we chose to prepare the atoms in a distance of $d \in \{-2, -1, 0, 1, 2\} \cdot \lambda/2$, where negative distances correspond to the cases in which the left atom crosses the position of the other atom on the right during the transport sequence. The cases $d \neq 0$ can in turn be used to quantitatively characterize the fidelity to bring both atoms into the same site. For each preparation distance we measured 300 repetitions which according to the discussion in section 4.2.2 results in approximately 150 initial patterns of two atoms in a distance of $25 \cdot \lambda/2$.

4.3.2 Results

In the following sections the results of the measurements will be analyzed and the on-site preparation efficiency will be estimated. We know from the previous sections that the single atom addressing fidelity A amounts to 86%. Therefore we expect that in $1 - A = 14\%$ of all attempts the addressing will fail and both atoms will remain in their initial positions. In the measurements we have observed this situation in approximately 13(2)% of all attempts and we have post-selected these events in all of the following analysis procedures.

The average intensity distribution of atoms in target separations of ± 2 , ± 1 , and 0 lattice sites allows for a qualitative cross-check of the obtained separation. Subsequently we conduct a quantitative study of the fidelity to prepare the atoms in a common site which is based on the mechanism of light-assisted collisions.

Two atom intensity distribution

For each preparation distance the fluorescence images which have been obtained after the preparation are summed pixel wise. The center of the images is defined by the reference position of the initial pattern. With this procedure we obtain the average intensity profile of two atoms which we expect to be prepared in the corresponding target distance. The resulting distributions in two and (vertically binned) in one dimension are shown in figure 4.14.

The vertically binned distributions are normalized to the highest integrated count rate and weighted with the number of images contributing to the summation. Due to the light-induced losses the relative height of the intensity distribution for two atoms prepared in a common site is significantly reduced. False preparations and one-atom losses (see section 4.3.3) still lead to a non-vanishing intensity profile. Using the intensity distributions one can already discriminate qualitatively between the different preparation distances. We observe that the center position of the intensity distributions shifts depending on the preparation distance from right to left in figure 4.14 (b).

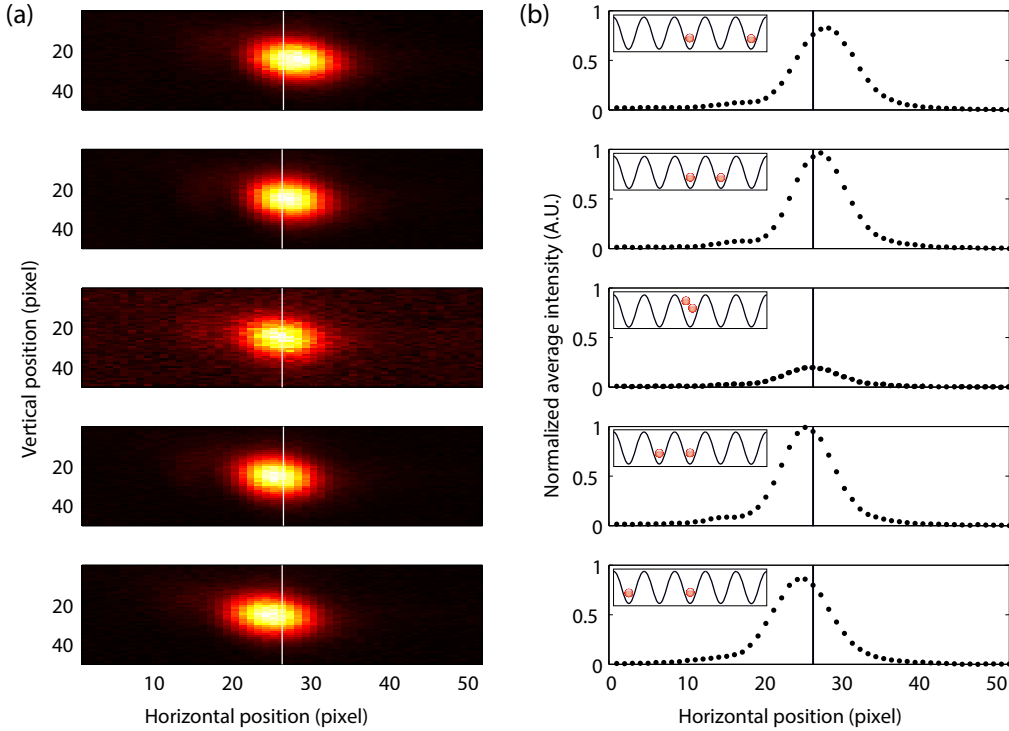


Figure 4.14: (a) Pixelwise summed fluorescence images, of two atoms prepared in target distances $d \in \{-2, -1, 0, 1, 2\} \cdot \lambda/2$ (from top to bottom). (b) Vertically integrated profile of the summed fluorescence images, normalized to the highest peak of all profiles. The inset shows the corresponding target preparation distance.

In addition we observe that the full width at half maximum (FWHM) of the intensity distributions for equal preparation distances is compatible and increases for further separated atoms

$$\Delta_{\text{FWHM}}(d = +1) = 7.92 \text{ pixel} \quad \Delta_{\text{FWHM}}(d = -1) = 7.99 \text{ pixel} \quad (4.6)$$

$$\Delta_{\text{FWHM}}(d = +2) = 8.88 \text{ pixel} \quad \Delta_{\text{FWHM}}(d = -2) = 8.85 \text{ pixel} \quad (4.7)$$

The integrated intensity profiles provide useful information for future benchmarks and improvements of numerical position reconstruction algorithms in the case of neighboring atoms. For this purpose we have so far relied on simulated fluorescence images but simulations can not cover all effects of the physical system. This is especially relevant as we have observed that the position reconstruction algorithm does so far not reliably detect the correct separation between neighboring atoms. Instead it seems to overestimate the actual distance systematically. An improved version of the current deconvolution algorithm has been developed by A. Alberti. It takes the discreteness of the lattice positions into account and based on simulated images promises better performance. In the future this algorithm will be tested on the given dataset.

4.3.3 Success rate of bringing two atoms to a common site

The interaction of two atoms in a common lattice site under illumination of the red-detuned fluorescence imaging beams leads to the mechanism of light-assisted collisions under which either one or both of the atoms escape from the optical lattice on a time-scale much shorter than the exposure time [50, 51]. This provides a clear signature to check whether both atoms have reached a single site without relying on position reconstruction methods. Hence, the analysis of the preparation efficiency will be based on this physical mechanism. A brief introduction into the physics of light-assisted collisions is given in the following paragraph. A detailed review of the topic can be found in [50].

Light-assisted collisions

In figure 4.15 (a) three molecular interaction potentials for atoms in the ground- or excited-state are depicted. These illustrate the two fundamental collision types, namely *radiative escape* and *fine-structure changing collisions*. In both cases an optical molasses photon with frequency $\hbar\omega_L$ (red-detuned to the D₂ transition) excites one of the two atoms to the $P_{3/2}$ state. As a consequence the interaction potential of the Cs₂ quasi-molecule changes from a short range *Van-der-Waals* interaction ($V(R) = -C_6/R^6$) to a long range *resonant dipole-dipole* interaction ($V(R) = -C_3/R^3$) [52].

Therefore the atoms attract each other and gain kinetic energy while moving on the potential curve. In the following either the excited state decays at interatomic distance R_{dec} by emitting a photon which is red-detuned with respect to ω_L , henceforth resulting in an overall kinetic energy gain per atom of

$$\Delta E_{\text{RE}} = (\hbar\omega_L - \hbar\omega_E(R_{\text{dec}}))/2.$$

This process is called *radiative escape*. Alternatively the excited atom undergoes a fine-structure change (fcc) at the crossing point of the $S_{1/2} + P_{3/2}$ and $S_{1/2} + P_{1/2}$ potentials which in turn leads to a gain in kinetic energy per atom of [53]

$$\Delta E_{\text{FCC}}/2k_B \approx 400 \text{ K}.$$

In this case both atoms immediately leave the trapping potential as the trap depth during the imaging process amounts to $U = 0.4 \text{ mK}$. In addition *hyperfine-structure changing collisions* (hcc) are possible during which, instead of a change in fine-structure, a change of the hyperfine-structure state occurs. The energy released in this case amounts to

$$\Delta E_{\text{HCC}}/2k_B \approx 10 \text{ mK}.$$

In conclusion, there are three loss mechanisms due to light-induced collisions. Out of these the *fine-* and *hyperfine-structure changing collisions* lead to an escape of both atoms as the energy gain is orders of magnitude larger than the depth of the trapping potential. The energy gain due to *radiative escape* has a continuous distribution. In section 4.3.4, I will argue that this process can in principle lead to the escape of only one atom, e.g. due to anisotropies in initial kinetic energies.

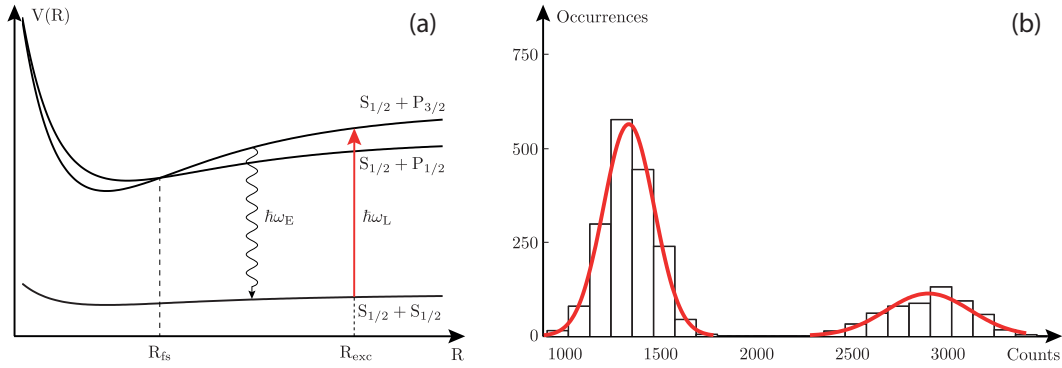


Figure 4.15: (a) Molecular interaction potentials as a function of interatomic distance R . (b) Histograms of integrated photoelectron counts of one and two atoms.

Determination of atom loss rates

In the following we extract the number of atoms that we observe after bringing the atoms to the target distance. Therefore, we have to ensure that we can clearly distinguish between two nearby atoms and a single one in terms of the integrated fluorescence counts. Figure 4.15 (b) shows a histogram of photoelectrons integrated over regions of interest in which the count-rate is significantly higher than the background. These have been observed in the fluorescence images before and after transporting both atoms to a target distance of $\pm 2, \pm 1$ and 0 lattice sites. The two distributions correspond to the contribution of one and two atoms, respectively. These are perfectly separated and hence we can reliably discriminate between zero, one and two remaining atoms by introducing suitable threshold conditions.

In principle three observations are possible. Either both atoms remain in the lattice (no atom loss), one atom remains (one atom loss) or none remains (two atoms loss). We have also observed detections of more than two atoms ($p = 1.6\%$). These are caused by atoms entering the field of view during transport or cosmic particles generating false counts on the detector. The events have been post-selected before the following analysis.

If no further loss channels, than those described by the single atom survival probability $S = 95\%$ (extracted in section 4.2.2), are present, we anticipate the bare loss rates for k out of two initially prepared atoms $L(k|2)$ to be given by

$$L(0|2) = S^2 = 90.3\% \quad (4.8)$$

$$L(1|2) = 2 \cdot (1 - S) \cdot S = 9.50\% \quad (4.9)$$

$$L(2|2) = (1 - S)^2 = 0.25\% \quad (4.10)$$

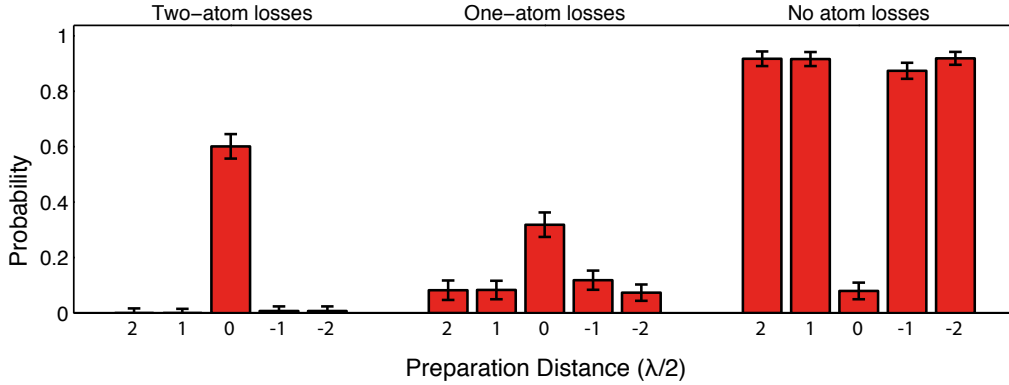


Figure 4.16: Observation of atom-losses after bringing two atoms to a distance $d \in \{-2 \cdot \lambda/2, -\lambda/2, 0, \lambda/2, 2 \cdot \lambda/2\}$. The confidence limits are obtained by the Clopper-Pearson method ($\alpha = 0.32$).

We expect light-induced losses to occur and modify these loss rates if both atoms have reached a common site. Hence, the efficiency and precision of the preparation manifests itself in a significant change of atom-loss rates for target distance $d = 0$ and unchanged loss rates for $d \neq 0$. Ideally (perfect preparation efficiency) at least one of the two atoms will be lost for $d = 0$, due to light-assisted collisions, which corresponds to $L(0|2) \rightarrow 0$. The observed atom loss rates for each preparation distance d are depicted in figure 4.16 and additionally listed in table 4.3.

For $d \neq 0$ the observations follow, within the uncertainties of the measurement, the predictions from the already extracted survival probability expressed by equations 4.8 - 4.10. In principle we expect the two-atom survival probability for $d = \pm 1$ to be slightly lower than for $d = \pm 2$ because in these cases there is a higher chance that position reconstruction or transport errors lead to a false preparation in $d = 0$. Based on the preparation efficiency in $d = 0$, we have estimated that this effect is on the order of the statistical uncertainties (3%) and can therefore not be reliably detected with the current sample size. The same is true for the expected increase of the two-atom loss rate due to false preparation in $d = 0$.

The loss rates for $d = 0$ differ significantly from those for $d \neq 0$ proving that atoms indeed reached the same lattice site and escaped the lattice due to light-induced collisions. The low residual survival probability of both atoms $L(0|2) = 8(3)\%$ indicates that the preparation efficiency is close to ideal. A detailed analysis of the preparation efficiency will follow in the next paragraph. Furthermore we observe one-atom losses which are significantly more probable from what can be explained by the limited survival probability. Hence, light-induced collisions presumably also lead to one-atom escapes in our system. A discussion of theoretical estimations and further experimental studies on the possible mechanism behind one-atom losses is presented in section 4.3.4.

Preparation distance d ($\lambda/2$)	Sample size	$L(2 2)$	$L(1 2)$	$L(0 2)$
2	109	0(2) %	8(4) %	92(3) %
1	120	0(2) %	8(3) %	92(3) %
0	138	60(4) %	32(4) %	8(3) %
-1	135	1(2) %	11(3) %	87(3) %
-2	136	1(2) %	7(3) %	92(2) %

Table 4.3: Observed two atom losses $L(2|2)$, one atom losses $L(1|2)$ and no atom losses $L(0|2)$ summarized for each preparation distance d . The confidence limits, given in brackets, were obtained with the Clopper-Pearson method ($\alpha = 0.32$).

Estimation of the preparation efficiency

In the following we want to estimate the preparation efficiency using the observed atom loss rates. The analysis will be based on the assumption that light-assisted collision can lead to one atom losses and that at least one atom leaves the optical lattice during fluorescence imaging if both atoms are successfully placed in a common site. Consequently, the observed rate of no atom loss $L(0|2)$ in case of $d = 0$ corresponds to unsuccessful preparation attempts.

Because of the limited survival probability S , the observed atom loss rates are a combination of atom losses due to light-assisted collisions $L_C(k|2)$ and bare atom losses $L_B(k|2)$ which are uncorrelated to a successful preparation

$$L(k|2) = L_B(k|2) + L_C(k|2).$$

By subtracting the theoretical estimates according to equations 4.8 - 4.10, of the bare one and two atom loss rates $L_B(k|2)$, we obtain an estimate of the loss rates due to on-site light-assisted collisions

$$L_C(k|2) = L(k|2) - L_B(k|2).$$

From these loss rates which are correlated to light-assisted collisions the on-site preparation efficiency for two atoms P_{success} can be estimated

$$P_{\text{success}} = L_C(1|2) + L_C(2|2) = 83(4) \%$$

This corresponds to a significant improvement of the previously reported preparation efficiency in our setup of $P = 37(8) \%$ [12] and a result employing crossed optical dipole traps with $P = 16(4) \%$ [44].

According to the previous analysis the preparation efficiency is currently limited by two effects. The bare two-atom survival probability reduces the probability that both atoms remain in the lattice during the preparation by about 9% (see equation 4.8). In addition the atoms might not reach the same site due to non-ideal position reconstruction or errors during transport (spin-flips, tunneling).

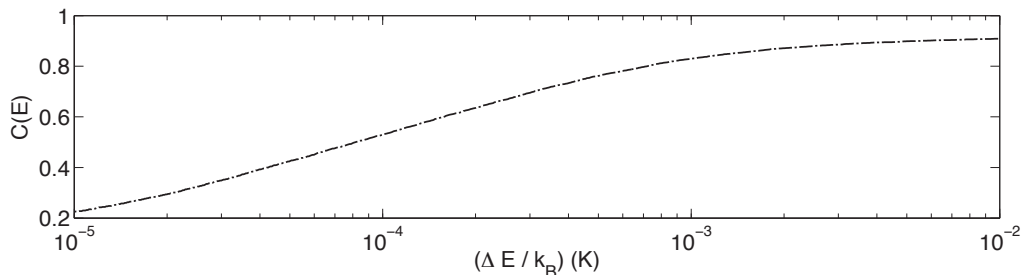


Figure 4.17: Cumulative distribution function $C(E)$ of the energy released per atom during light-assisted collisions according to the Monte Carlo simulation discussed in the text.

4.3.4 Discussion of light-induced one atom losses

Energy release during radiative escape

As the gain in kinetic energy during light-assisted collisions is symmetrically distributed between the collision partners the observation of one-atom losses can only be explained by anisotropies in the initial energy of the atoms or of the trapping geometry. These anisotropies only have an impact if the energy released during the collision is below or on the order of the trapping potential. We have estimated that the process of *fine-structure* or *hyperfine-structure changing collisions* releases significantly more energy than the trap depth. Hence, only the process of radiative escape can lead to one-atom losses.

In the following I will describe a simple theoretical estimation of the energy released during *radiative escape*. The calculations are implemented as a Monte-Carlo simulation based on deliberations by Pritchard and Gallagher [54] and by Kuhr [53]. We assume that the pair of atoms is initially excited at the Condon point R_0 which is defined by [55]

$$V_{S+P}(R_0) = \hbar\delta,$$

with $\delta < 0$ being the detuning, of the optical molasses beam that illuminates the atoms during imaging, to the D_2 line. The detuning in our setup is given by $\delta = 7\Gamma$ [14]. The potential V_{S+P} is approximated by a model from Meath [56]

$$V_{S+P}(R) = -f \hbar \Gamma_{D_2} \left(\frac{\lambda_{D_2}}{2\pi R} \right)^3, \quad (4.11)$$

where f is a factor close to unity [50], $\Gamma_{D_2} = 2\pi \times 5.22$ MHz is the natural linewidth of the D_2 line, and $\lambda_{D_2} = 852.347$ nm is the corresponding transition wavelength. The classical equation of motion in one dimension with reduced mass of the two-body system $\mu = M_{Cs}/2$

$$\mu \frac{d^2}{dt^2} R(t) = -\frac{\partial V_{S+P}}{\partial R}, \quad (4.12)$$

is numerically solved with temporal discretization $\Delta t = 10^{-12}$ s $\ll 1/\Gamma_{D2}$ and the initial conditions

$$R(t=0) = R_0, \quad \left. \frac{d}{dt}R \right|_{t=0} = 0.$$

Using the differential equation we simulate the evolution of the system in the following way. At each time-step the excited state decays with probability $1 - \exp(-\Delta t \Gamma_{D2})$. If this is the case, we store the current position of the quasi-molecule and convert it into the energy gain per atom via

$$\Delta E = (V(R_0) - V(R))/2.$$

In the opposite case we update the distance of the atoms according to the numerical solution of the equation of motion and enter the next time-step until at some point the excited state decays. We repeat the procedure for 10^6 realizations to reduce the statistical uncertainties. Afterwards we generate the cumulative distribution function $C(E)$ of the energy gain by determining the fraction of atoms that obtained an energy gain smaller than E . The resulting distribution is shown in figure 4.17.

According to the simulation approximately 70% of the collisions lead to an energy gain per atom which is less than the trap depth. This indicates that *radiative escape* collisions are in principle sensitive to the initial energy of the atoms and therefore can lead to one atom losses. The cumulative distribution function does not reach unity because in approximately 10% of the simulations the interatomic distance becomes smaller than the validity region of the assumed potential. In these cases the repulsive *van der Waals* interaction and the centrifugal barrier lead to an oscillation on the potential curve that is not treated here. Hence, no prediction on the energy release of these events can be given. In addition, a more precise calculation would require to average over the molecular potential curves. Further, no estimation of the relative occurrence of the different collision types is available, although theoretical calculations predict them to be equally probable [50].

Further experimental studies

Light-assisted collisions leading to a one-atom loss have been reported in a previous configuration of our setup. In that case a non-deterministic method to prepare two atoms in a common lattice site has been used and a branching ratio of one and two-atom losses of 46:54 has been reported [12]. A possible explanation for the different branching ratio is that the configuration of the lattice beams and the cooling laser frequencies has changed significantly over the years and theoretical studies have proven that this leads to significant variations in the branching ratio.

Further measurements with two Cesium atoms prepared in a micro-potential via two crossed optical dipole traps also suggested the existence of one atom losses [57] and even measurements in a few atom Cesium MOT have lead to their observation [53, 55, 58]. In addition, theoretical calculations and experimental results have confirmed similar findings in a system of Rubidium atoms [52].

4.3.5 Conclusion

In conclusion, we have realized a feedback method that allows us to prepare two atoms in a common lattice site with a high preparation efficiency of $P = 83(4)\%$. The observation of significantly increased atom loss rates due to light-assisted collisions provide a direct method to estimate the preparation efficiency. We have observed light-induced one-atom losses and theoretical estimations have been presented which indicate that the collision mechanism of *radiative escape* can lead to such observations due to anisotropies in the initial energy of the atoms or the trapping potential. The results pave the way for future experiments intended to study controlled interactions or interferences between precisely two atoms.

5 Summary and Outlook

In this thesis, I have presented feedback methods to generate arbitrary patterns of atoms in an one-dimensional, spin-dependent optical lattice. For this purpose a new control software for the experiment has been planned and implemented. It encapsulates experimental control, acquisition of fluorescence images, and their analysis into a single program and thereby allows for the realization of feedback logic.

Based on a versatile and adaptive feedback algorithm we have arranged equidistant strings of up to six atoms with interatomic separation of $d \geq 20$ lattice sites. The measured preparation efficiency agrees with predictions of a theoretical model indicating that the relevant technical limitations have been identified. In future experiments the pattern generation method can be applied to arrange starting distributions for interacting quantum walks or even multi-qubit gate arrays.

The main result of this work is the precise preparation of two atoms in a common lattice site. After preparing two atoms in a well-defined initial separation, employing the feedback algorithm mentioned above, both atoms have been transported into the same lattice site. We induced light-assisted collisions between atoms that reached a common site and estimated the preparation efficiency based on the observed light-induced loss rates, yielding 83(4) %. This represents a significant improvement compared to previous results obtained in our group.

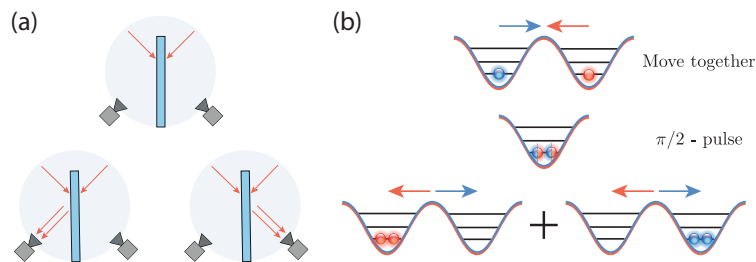


Figure 5.1: (a) The Hong-Ou-Mandel experiment: Two indistinguishable photons impinging on the input ports of a beam splitter show bunching at the output due to interference. (b) Analogous implementation with massive Cesium atoms prepared in the motional ground-state. Both atoms are spin-dependently transported into a common lattice site. A $\pi/2$ -pulse removes the which-way information leading to bunched observation of both atoms when separating the spin-dependent potentials.

During the work presented in this thesis the experimental setup has been extended with an additional doughnut-shaped and blue-detuned trap leading to a stronger confinement of the atoms in the transversal directions. Combined with a Raman laser system resolved-sideband cooling of the transversal motion has been observed, enabling the preparation of atoms in the three-dimensional ground-state [25]. The combination of position feedback and ground-state cooling opens the door for the study of fascinating physics from the Hong-Ou-Mandel interference of two indistinguishable massive particles (shown in figure 5.1) to the realization of a fundamental two-qubit gate.

Bibliography

- [1] Y. Manin, “Computable and noncomputable,” *Sov.Radio.*, pp. 13–15, 1980.
- [2] R. P. Feynman, “Simulating physics with computers,” *International Journal of Theoretical Physics*, vol. 21, no. 6-7, pp. 467–488, 1982.
- [3] M. Nielsen and I. Chuang, *Quantum Computation and Quantum Information*. Cambridge University Press, 2000.
- [4] I. Deutsch, G. Brennen, and P. Jessen, “Quantum computing with neutral atoms in an optical lattice.” arXiv preprint quant-ph/0003022.
- [5] J. I. Cirac and P. Zoller, “Quantum computations with cold trapped ions,” *Phys. Rev. Lett.*, vol. 74, no. 4091, 1995.
- [6] A. Arkhipov and S. Aaronson, “The computational complexity of linear optics.” preprint <http://arxiv.org/abs/1011.3245>.
- [7] A. Blais, R. Huang, A. Wallraff, S. Girvin, and R. Schoelkopf, “Cavity quantum electrodynamics for superconducting electrical circuits: An architecture for quantum computation,” *Phys. Rev. A*, vol. 69, no. 062320, 2004.
- [8] C. Monroe, D. Meekhof, B. King, W. Itano, and D. Wineland, “Demonstration of a fundamental quantum logic gate,” *Phys. Rev. Lett.*, vol. 75, pp. 4714–4717, 1995.
- [9] T. Monz, P. Schindler, J. Barreiro, M. Chwalla, D. Nigg, W. Coish, M. Harlander, W. Haensel, M. Henrich, and R. Blatt, “14-qubit entanglement: creation and coherence,” *Phys. Rev. Lett.*, vol. 106, no. 130506, 2011.
- [10] D. Jaksch, J. I. Cirac, P. Zoller, S. L. Rolston, R. Côté, and M. D. Lukin, “Fast quantum gates for neutral atoms,” *Phys. Rev. Lett.*, vol. 85, pp. 2208 – 2211, 2000.
- [11] O. Mandel, M. Greiner, A. Widera, T. Rom, T. Hänsch, and I. Bloch, “Controlled collisions for multi-particle entanglement of optically trapped atoms,” *Nature*, vol. 425, p. 937, 2004.
- [12] M. Karski, *State-selective transport of single neutral atoms*. PhD thesis, University of Bonn, 2010.
- [13] L. Förster, *Microwave control of atomic motion in a spin dependent optical lattice*. PhD thesis, University of Bonn, 2010.

- [14] A. Steffen, *Single atom interferometers and Bloch oscillations in quantum walks*. PhD thesis, University of Bonn, 2013.
- [15] E. L. Raab, M. Prentiss, A. Cable, S. Chu, and D. Pritchard, “Trapping of neutral sodium atoms with radiation pressure,” *Phys. Rev. Lett.*, vol. 59, no. 23, pp. 2631–2634, 1987.
- [16] H. J. Metcalf and P. van der Straten, *Laser cooling and trapping*. Springer, 1999.
- [17] X. Baillard, A. Gauguier, S. Bize, P. Lemonde, P. Laurent, A. Clairon, and P. Rosenbusch, “Interference-filter-stabilized external-cavity diode lasers.” arXiv:0605046v1, 2006.
- [18] C. Robens and A. Alberti private communication, 2014.
- [19] F. Bloch, “Nuclear induction,” *Phys. Rev.*, vol. 70, pp. 460–474, 1946.
- [20] M. Karski, L. Förster, J. Choi, A. Steffen, W. Alt, D. Meschede, and A. Widera, “Quantum Walk in Position Space with Single Optically Trapped Atoms,” *Science*, vol. 325, p. 174, 1996.
- [21] A. Steffen, A. Alberti, W. Alt, N. Belmechri, S. Hild, M. Karski, A. Widera, and D. Meschede, “A digital atom interferometer with single particle control on a discretized spacetime geometry,” *PNAS*, vol. 109, p. 9770, 2012.
- [22] D. Döring, “Ein Experiment zum zustandsabhängigen Transport einzelner Atome,” Master’s thesis, University of Bonn, 2007.
- [23] D. A. Steck, “Cesium D Line Data,” 1998.
- [24] A. Hambitzer, “Direct Synthesis of Light Polarization for State-Dependent Transport,” Master’s thesis, University of Bonn, 2012.
- [25] C. Robens, *to be published*. PhD thesis, University of Bonn, 2015.
- [26] E. Abbe, “Beiträge zur Theorie des Mikroskops und der mikroskopischen Wahrnehmung,” *Archiv für mikroskopische Anatomie*, vol. 9, no. 1, pp. 413–468, 1873.
- [27] H. Helmholtz, “On the limits of the optical capacity of the microscope,” *The monthly microscopical journal*, vol. 16, no. 1, pp. 15–39, 1876.
- [28] Waseem S. Bakr, and Jonathon I. Gillen, and Amy Peng, and Simon Fölling, and Markus Greiner, “A quantum gas microscope for detecting single atoms in a hubbard-regime optical lattice,” *Nature*, vol. 462, p. 74, 2009.
- [29] J. F. Sherson, C. Weitenberg, M. E. M. Cheneau, I. Bloch, and S. Kuhr, “Single-atom-resolved fluorescence imaging of an atomic mott insulator,” *Nature*, vol. 467, p. 68, 2010.

-
- [30] F. Kleiβler, “Assembly and Characterization of a High Numerical Aperture Microscope for Single Atoms,” Master’s thesis, University of Bonn, 2014.
- [31] M. Karski, L. Förster, J. Choi, W. Alt, A. Widera, and D. Meschede, “Nearest-Neighbor Detection of Atoms in a 1D Optical Lattice by Fluorescence Imaging,” *Phys. Rev. Lett.*, vol. 102, p. 053001, 1996.
- [32] S. Kuhr, *A controlled quantum system of individual neutral atoms*. PhD thesis, University of Bonn, 2003.
- [33] D. Jaksch, H.-J. Briegel, J. I. Cirac, C. W. Gardiner, and P. Zoller, “Entanglement of atoms via cold controlled collisions,” *Phys. Rev. Lett.*, vol. 82, pp. 1975 – 1978, 1999.
- [34] S. Hild, “Resolved Raman sideband cooling in a doughnut-shaped optical trap,” Master’s thesis, University of Bonn, 2011.
- [35] L. Förster, M. Karski, J. Choi, A. Steffen, W. Alt, D. Meschede, A. Widera, E. Montano, J. H. Lee, W. Rakreungdet, and P. S. Jessen, “Microwave Control of Atomic Motion in Optical Lattices,” *Phys. Rev. Lett.*, vol. 103, p. 233001, 2009.
- [36] M. Karski, L. Förster, J. Choi, A. Steffen, N. Belmechri, W. Alt, D. Meschede, and A. Widera, “Imprinting Patterns of Neutral Atoms in an Optical Lattice using Magnetic Resonance Techniques,” *New J. Phys.*, vol. 12, p. 065027, 1996.
- [37] D. Schrader, *A Neutral Atom Quantum Register*. PhD thesis, University of Bonn, 2004.
- [38] D. Kim, “Quantum Register Initialization via Deterministic Atom Sorting in Optical Lattices,” Master’s thesis, University of Bonn, 2012.
- [39] W. Setiawan, *Fermi Gas Microscope*. PhD thesis, Harvard University, 2012.
- [40] A. Keshet and W. Ketterle, “A Distributed GUI-based Computer Control System for Atomic Physics Experiments,” *Rev. Sci. Instrum.*, vol. 84, no. 015105, 2013.
- [41] Analog Devices, *AD9954 datasheet*, 2014.
- [42] M. Genske, “Electric Quantum Walks with Individual Atoms,” Master’s thesis, University of Bonn, 2012.
- [43] A. J. Nelder and R. Mead, “A simplex method for function minimization,” *Computer Journal*, vol. 7, pp. 308–313, 1965.
- [44] Y. Miroshnychenko, W. Alt, I. Dotsenko, L. Förster, M. Khudaverdyan, D. Meschede, D. Schrader, and A. Rauschenbeutel, “An atom-sorting machine,” *Nature*, vol. 442, p. 151, 2006.

- [45] Y. Miroshnychenko, *An atom-sorting machine*. PhD thesis, University of Bonn, 2006.
- [46] T. Calarco, H.-J. Briegel, D. Jaksch, J. I. Cirac, and P. Zoller, “Entangling neutral atoms for quantum information processing,” *J. Mod. Opt.*, vol. 47, no. 12, pp. 2137 – 2149, 2000.
- [47] D. Schrader, I. Dotsenko, M. Khudaverdyan, Y. Miroshnychenko, A. Rauschenbeutel, and D. Meschede, “Neutral Atom Quantum Register,” *Phys. Rev. Lett.*, vol. 93, p. 150501, 2004.
- [48] C. Weitenberg, M. Endres, J. F. Sherson, M. Cheneau, P. Schauß, T. Fukuhara, I. Bloch, and S. Kuhr, “Single-spin addressing in an atomic mott insulator,” *Nature*, vol. 471, p. 319, 2011.
- [49] M. Khudaverdyan, W. Alt, I. Dotsenko, L. Förster, S. Kuhr, D. Meschede, Y. Miroshnychenko, D. Schrader, and A. Rauschenbeutel, “Adiabatic Quantum State Manipulation of Single Trapped Atoms,” *Phys. Rev. A*, vol. 71, p. 031404, 2005.
- [50] J. Weiner, V. S. Bagnato, S. Zilio, and J. P. S., “Experiments and theory in cold and ultracold collisions,” *Reviews of Modern Physics*, vol. 71, no. 1, 1999.
- [51] C. Weitenberg, *Single-atom resolved imaging and manipulation in an atomic mott insulator*. PhD thesis, TU Munich, 2011.
- [52] P. Sompet, A. Carpentier, Y. Fung, M. McGovern, and M. Andersen, “Dynamics of two atoms undergoing light-assisted collisions in an optical microtrap,” *Phys. Rev. A*, vol. 88, p. 051401, 2013.
- [53] S. Kuhr, “Kalte Stöße mit einzelnen Atomen,” Master’s thesis, University of Bonn, 1999.
- [54] A. Gallagher and D. E. Pritchard, “Exoergic collisions of cold Na-Na,” *Phys. Rev. Lett.*, vol. 63, no. 9, pp. 957–960, 1989.
- [55] B. Ueberholz, S. Kuhr, D. Frese, V. Gomer, and D. Meschede, “Cold collisions in a high-gradient magneto-optical trap,” *J. Phys. B: At. Mol. Opt. Phys.*, vol. 35, p. 4899, 2002.
- [56] W. J. Meath, “Retarded interaction energies between like atoms in different energy states,” *The Journal of Chemical Physics*, vol. 48, no. 227, pp. 228–235, 1968.
- [57] Y. Miroshnychenko, W. Alt, I. Dotsenko, L. Förster, M. Khudaverdyan, D. Meschede, S. Reick, and A. Rauschenbeutel, “Inserting two atoms into a single optical micropotential,” *Phys. Rev. Lett.*, vol. 97, p. 243003, 2006.
- [58] B. Ueberholz, S. Kuhr, D. Frese, D. Meschede, and V. Gomer, “Counting Cold Collisions,” *J. Phys. B: At. Mol. Opt. Phys.*, vol. 33, 2000.

Acknowledgements

Nach einem sehr intensiven und spannenden Jahr möchte ich mich bei folgenden Personen bedanken:

- bei Professor Meschede für die Möglichkeit, an einem faszinierenden Experiment arbeiten zu dürfen und für die Betreuung als BCGS Mentor.
- bei Professor Kroha für die Übernahme des Zweitgutachtens.
- bei Dr. Andrea Alberti und Dr. Wolfgang Alt für viele hilfreiche Diskussionen und ihre umfassende Betreuung (Andrea danke ich außerdem für das Korrekturlesen dieses Texts und Wolfgang für die Teepausen).
- bei Carsten Robens für eine tolle Zusammenarbeit im Labor, die mir sehr viel Freude gemacht hat, außerdem für die umfangreichen Korrekturvorschläge für den vorliegenden Text und mein Masterkolloquium.
- bei Stefan Brakhane für die Betreuung während des Praktikums vor Beginn meiner Masterarbeit und für die Tipps für mein Masterkolloquium.
- bei Stanislav Shestovy, für die gegenseitige Motivation auf den letzten Metern.
- bei meinen Bürokameraden : Jose, Ricardo, Felix, Stefan, Carsten, Isabelle - It was always nice working with you.
- bei Anneliese, Fien und Dietmar für ihre Hilfe bei organisatorischen Problemen.

Declaration

I hereby declare that this thesis was formulated by myself and that no sources or tools other than those cited were used.

Bonn, 29.09.2014
